Chapter 11

Stress–Strain Models

Buddhism statue in Sukhothai, Thailand.
Sukhothai was the capital of the first Thai kingdom within the present territory of Thailand. Buddhism flourished in this capital. Sukhothai Kingdom reached its peak in late thirteenth Century under the reign of King Ramkhamhaeng. After him, however, Sukhothai declined quickly and came under control of Ayutthaya Dynasty in late fourteenth Century.

11.1 Hyperbolic and Ramberg–Osgood Stress–Strain Models

Stress–strain relationship of soil is characterized by the rigidity when strain is small as well as the shear strength at large strains, which is the upper bound of the stress level. This fundamental nature of soil behavior has often been modeled by a hyperbolic curve (Fig. 11.1); refer to Kondner (1963) together with Kondner and Zelasko (1963).

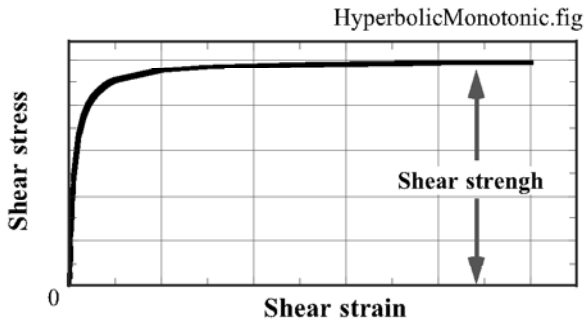

Fig. 11.1 Hyperbolic modeling of stress-strain behavior subjected to monotonic shear

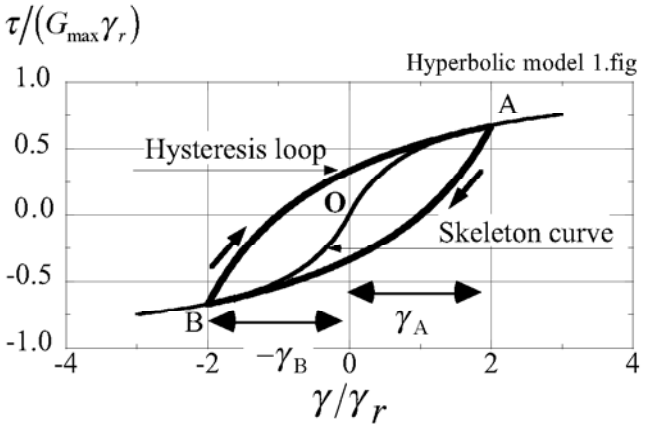

Fig. 11.2 Hyperbolic stress–strain model for cyclic loading

It is possible to model a cyclic stress–strain curve by a hyperbola as well. This model is used for dynamic analyses in the time domain. In case of *an analysis on a one-dimensional (level) ground* subjected to horizontal shaking,

$$\tau = \frac{G_{\max}\gamma}{1+\left|\gamma/\gamma_{\mathrm{r}}\right|}, \qquad (11.1)$$

in which G_{max} is the shear modulus at a very small strain amplitude, while a parameter of γ_{r} is called the reference strain. Since

$$\tau \to G_{\max}\gamma_r \quad \text{when} \quad \gamma \to \infty,$$

γ_r stands somehow for shear strength property.

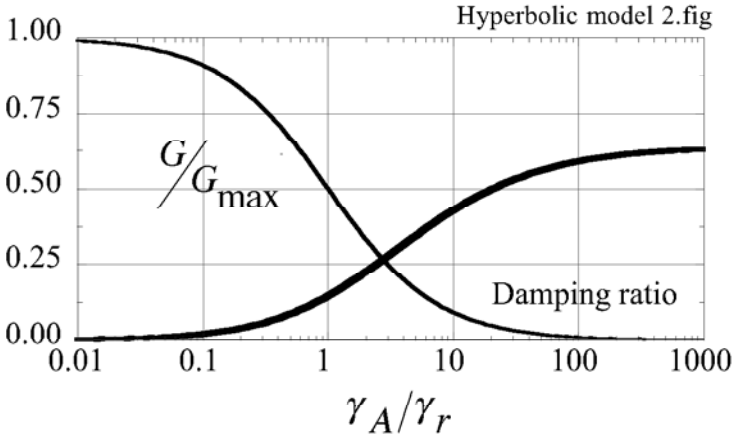

Fig. 11.3 G and h of hyperbolic model

The hyperbolic equation (11.1) models the skeleton curve BOA in Fig. 11.2. The skeleton curve is the one that passes through the ends of hysteresis loop with a variety of strain amplitude $\pm\gamma_{\mathrm{A}}$ (Fig. 11.2). Equation (11.2) gives a formula for secant modulus, G, varying with the strain amplitude,

$$\frac{G}{G_{\max}} = \frac{\tau/\gamma}{G_{\max}} = \frac{1}{1+\left|\gamma_{\mathrm{A}}/\gamma_{\mathrm{r}}\right|}. \qquad (11.2)$$

The hysteresis loop, A⇒B⇒A in Fig. 11.2, is often modeled by enlarging the skeleton curve two times (Masing rule: Masing, 1926);

$$\frac{\tau-\tau_{\mathrm{A}}}{2} = \frac{G_{\max}\dfrac{\gamma-\gamma_{\mathrm{A}}}{2}}{1+\left|(\gamma-\gamma_{\mathrm{A}})/(2\gamma_{\mathrm{r}})\right|} \quad \text{for A⇒B} \quad \text{and} \quad \frac{\tau-\tau_{\mathrm{B}}}{2} = \frac{G_{\max}\dfrac{\gamma-\gamma_{\mathrm{B}}}{2}}{1+\left|(\gamma-\gamma_{\mathrm{B}})/(2\gamma_{\mathrm{r}})\right|} \quad \text{for B⇒A,}$$

where $\gamma_{\mathrm{B}} = -\gamma_{\mathrm{A}}$ and $\tau_{\mathrm{B}} = -\tau_{\mathrm{A}}$ as shown by (11.1). The damping ratio is obtained by calculating W and

ΔW (area of loop):

$$W = \frac{G\gamma_A{}^2}{2} = \frac{G_{max}\gamma_A{}^2}{2(1+\gamma_A/\gamma_r)} \tag{11.3}$$

$$\Delta W = 2\int_{-\gamma_A}^{\gamma_A} (\text{Hysteresis loop B} \Rightarrow \text{A})\, d\gamma = 2\int_{-\gamma_A}^{\gamma_A} \left\{ \tau_B + \frac{G_{max}(\gamma - \gamma_B)}{1+\left|(\gamma-\gamma_B)/(2\gamma_r)\right|} \right\} d\gamma \tag{11.4}$$

$$= 2\int_{-\gamma_A}^{\gamma_A} \left\{ -\frac{G_{max}\gamma_A}{1+\gamma_A/\gamma_r} + \frac{G_{max}(\gamma+\gamma_A)}{1+(\gamma+\gamma_A)/(2\gamma_r)} \right\} d\gamma = \frac{4G_{max}}{1+\gamma_A/\gamma_r}\frac{\gamma_A}{\gamma_r}\left(\frac{\gamma_A}{\gamma_r}+2\right) - 8G_{max}\gamma_r{}^2 \log_e\left(1+\frac{\gamma_A}{\gamma_r}\right) \tag{11.5}$$

$$\text{Damping ratio, } h = \frac{2}{\pi}\left\{ \left(1+\frac{2}{\gamma_A/\gamma_r}\right) - 2\frac{1+\dfrac{\gamma_A}{\gamma_r}}{(\gamma_A/\gamma_r)^2} \log_e\left(1+\frac{\gamma_A}{\gamma_r}\right) \right\} \tag{11.6}$$

Figure 11.3 demonstrates the relationship of G/G_{max} and h with the strain amplitude. It should be noted that the reference strain is the strain amplitude at which $G/G_{max} = 0.5$. The damping ratio at a very large strain amplitude approaches $2/\pi = 0.637$, which is much larger than what is reported by experiments (Chap. 10). Thus, the hyperbolic model should not be used in a large-strain range. Although its idea is clear, the hyperbolic model cannot freely adjust the shape of curves. Hence, experimental results cannot be fully considered. This problem is avoided in an equivalent-linear approach (Sect. 9.10) by using a model by Hardin and Drnevich (1972):

$$\text{Damping ratio, } h = \text{Maximum damping ratio at large strain} \times \left(1 - G/G_{max}\right)$$

in which G/G_{max} at a given strain amplitude is derived from (11.2).

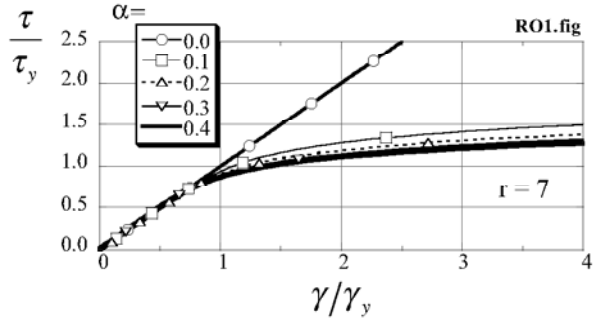

Fig. 11.4 Variation of skeleton curve with α

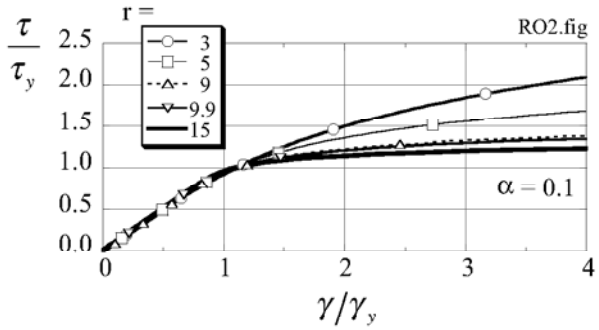

Fig. 11.5 Variation of skeleton curve with changing r.

The Ramberg–Osgood model is another kind of idea that reproduces the one-dimensional stress–strain behavior in the course of cyclic shear. Jennings (1964) used this model in terms of force and displacement. This text, however, describes the skeleton curve of this model by means of stress and strain:

$$\frac{\gamma}{\gamma_y} = \frac{\tau}{\tau_y}\left\{ 1 + \alpha\left(\frac{\tau}{\tau_y}\right)^{r-1} \right\} \tag{11.7}$$

in which a subscript "y" means characteristic values, while α and r are soil parameters to be determined by soil testing. Figures 11.4 and 11.5 illustrate the variation of curves by (11.7) with changing parameters:

The major features of this model as compared with the hyperbolic model are as what follows.

1. There is no upper bound in shear stress; i.e., $\lim_{\gamma \to \infty} \tau$ is infinite. Therefore, shear strength is not considered. As an alternative, soil parameters in the model are adjusted to make shear stress at 1% strain, for example, equal to an appropriate value.
2. Since there are three parameters, there is more freedom to take into account the complex soil behavior; for example, shear modulus at small strain, damping ratio at large strain, and shear stress at large strain.
3. Equation (11.7) helps calculate the strain value from a given value of stress. Shear stress, conversely, cannot be directly calculated from strain. This may make a nonlinear analysis more time consuming because stress determination needs iteration.

Both hyperbolic and Ramberg–Osgood models are intended to be used for a single-degree-of-freedom situation. Therefore, horizontal shaking of a level ground is their major target. Extension to a multi-dimensional situation needs more elaborate modeling.

Deformation of soil is characterized by dilatancy, which is the volume change induced by shear deformation (Sect. 1.6). Under cyclic loading, the volume change occurs as contraction, which means subsidence of ground surface after an earthquake event (Sect. 17.11). It will be shown later that the volume contraction in drained condition is equivalent with the development of excess pore water pressure in undrained conditions (Sect. 18.1). This is the cause of liquefaction and extensive damage.

Figure 11.6 illustrates an example of a drained cyclic shear test with a constant amplitude of strain conducted by a torsion shear apparatus (Sect. 18.8). The density of the tested sand was medium (relative density = 56%). It is first observed that the stress amplitude increases as the number of cyclic loading increases (see Fig. 10.6 as well). This implies that stiffness of soil increases with the progress of drained cyclic loading. Second, the net volumetric strain is contractive, accumulating toward 5% or more, although dilatant behavior is still observed when the shear strain exceeds 0.7%. Figure 11.7 illustrates more detailed variation of volumetric strain in one cycle in which both contraction and dilation occur in different phases of deformation.

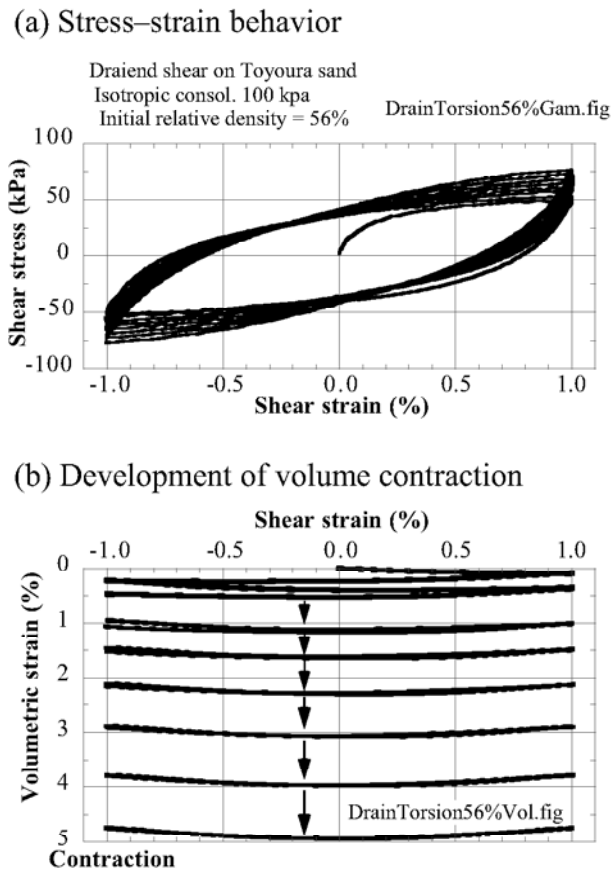

Fig. 11.6 Drained cyclic shear test (Dr = 56%) (Shahnazari and Towhata, 2002)

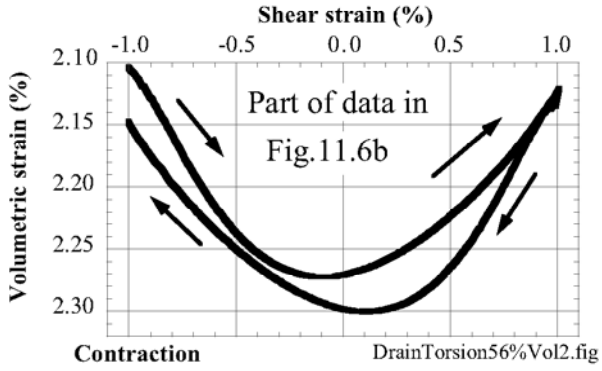

Fig. 11.7 Accumulation of volumetric strain in one cycle of loading (data from Shahnazari and Towhata, 2002)

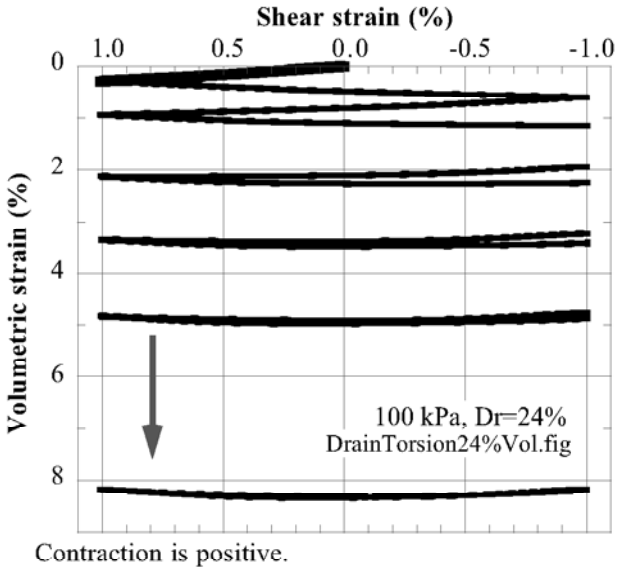

Fig. 11.8 Volume change of very loose sand (Dr = 24%) (Shahnazari and Towhata, 2002)

Figure 11.8 indicates the volume contraction of looser sand. Although the consolidation stress and strain amplitude are identical with the data in Fig. 11.6, the accumulation of volume change occurred faster.

As mentioned in Sect. 1.6, the dilatant behavior of sand has been investigated by many people by using the so-called stress-dilatancy relationship:

$$\frac{\tau}{\sigma'} = K\left(-\frac{\mathrm{d}\varepsilon_{\mathrm{v}}}{\mathrm{d}\gamma_{\mathrm{p}}}\right) + \text{constant} \qquad (11.8)$$

in which ε_{v} designates the volumetric strain (positive in compression). Positive and negative dilatancy is reproduced in accordance with positive and negative values of $\mathrm{d}\varepsilon_{\mathrm{v}}/\mathrm{d}\gamma_{\mathrm{p}}$. Moreover, the present section employs γ_{p}, which is the plastic (irrecoverable) component of shear strain. The stress dilatancy relationship of sand undergoing cyclic loading was studied by Pradhan et al. (1989) and later by Hinokio et al. (2001). The present study, in contrast, attempts to indicate the stress-dilatancy behavior of sand subjected to more number of cycles.

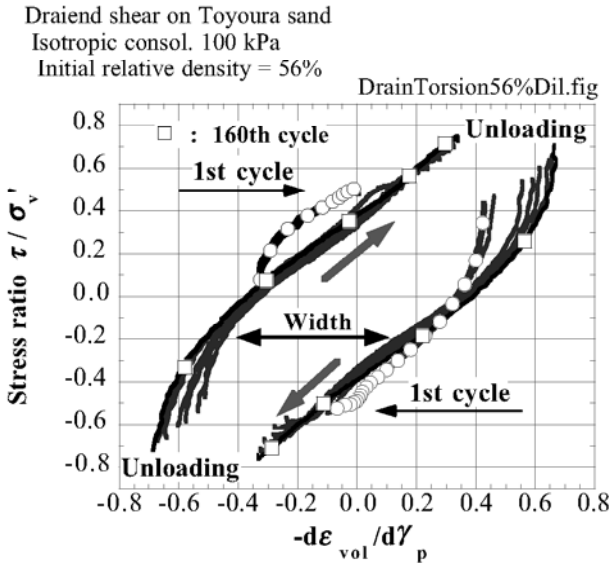

Fig. 11.9 Stress-dilatancy relationship of sand with relative density = 56% (Shahnazari and Towhata, 2002)

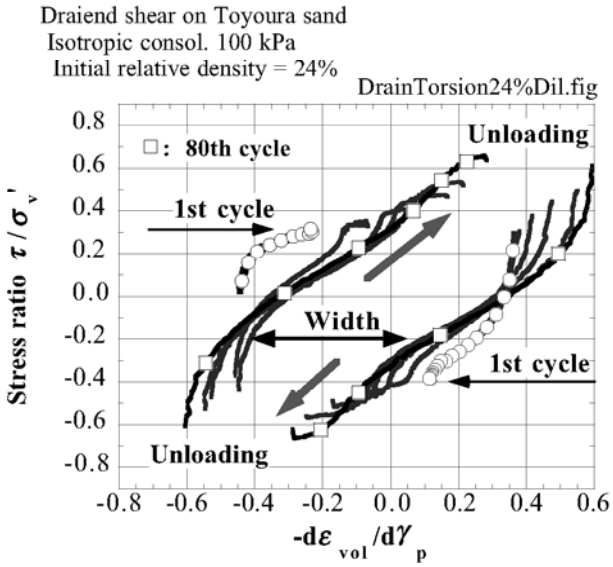

Fig. 11.10 Stress-dilatancy relationship of sand with relative density = 24% (Shahnazari and Towhata, 2002)

Figures 11.9 and 11.10 reveal two stress-dilatancy diagrams that were obtained by tests with relative densities of 56% and 24%, respectively. The employed number of loading cycles was 160 and 80, and the relative density was increased by cyclic loading to 80% and 69%, respectively. Only data from selected cycles was plotted in the figures. Note that $-\mathrm{d}\varepsilon_{\mathrm{vol}}/\mathrm{d}\gamma_{\mathrm{p}} < 0$ means volume contraction when the stress ratio, $\tau/\sigma_{\mathrm{v}}'$, is increasing and vice versa. From these diagrams, the following points may be made:

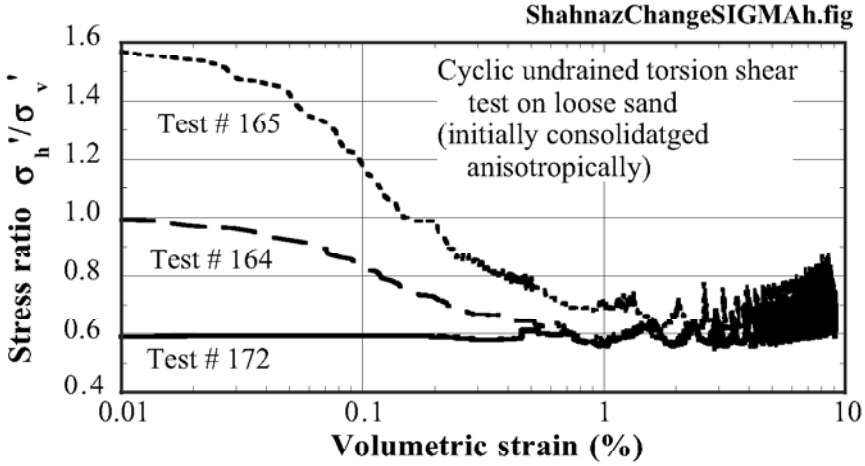

Fig. 11.11 Reduction of lateral earth pressure coefficient due to cyclic drained loading (Shahnazari and Towhata, 2002)

1. Although the density of sand affects the range of mobilized (activated) stress level, the range of dilatancy ratio, $-\mathrm{d}\varepsilon_{\mathrm{vol}}/\mathrm{d}\gamma_{\mathrm{p}}$, is not much affected.

2. There is an approximate linearity in the stress–dilatancy relationship.
3. $-\mathrm{d}\varepsilon_{\mathrm{vol}}/\mathrm{d}\gamma_{\mathrm{p}}$ jumps upon the initiation of unloading as reported by Pradhan et al. (1989).
4. The first cycle of loading exhibits greater values of $\left|-\mathrm{d}\varepsilon_{\mathrm{vol}}/\mathrm{d}\gamma_{\mathrm{p}}\right|$, which imply greater tendency for volume contraction.
5. Immediately after the onset of unloading (change of loading direction), $-d\varepsilon_{vol}/d\gamma_{p}$ exhibits volume contraction. This tendency increases as the number of loading cycles increases.
6. Conversely towards the end of loading (before unloading), $-\mathrm{d}\varepsilon_{\mathrm{vol}}/\mathrm{d}\gamma_{\mathrm{p}}$ shows greater values (more dilatancy), making the width of stress–dilatancy loop smaller; for definition of "width", see the figures.

Volume contraction as a consequence of cyclic shear results not only in ground subsidence but also in lateral contraction. In a horizontal ground where lateral strain is confined to zero, the potential contraction in the horizontal direction causes reduction of lateral earth pressure. Figure 11.11 is an experimental evidence of this phenomenon, which was obtained by torsion shear tests. This finding implies reduction of lateral earth pressure coefficient at rest (K_0).

11.3 Theory of Elastoplasticity

Hyperbolic and Ramberg–Osgood models in Sect. 11.1 presented relationships between shear stress and strain, which are useful in dynamic analyses on horizontal ground. Since only one component of stress and one component of strain are therein studied, however, those models cannot be applied to two- or three-dimensional analyses in which many components of stress and strain are involved.

The elastoplastic modeling is one of the widely employed approaches to multi-dimensional modeling in which an increment of strain, $d\varepsilon$, induced by stress increments is decomposed into elastic and plastic components;

$$d\varepsilon = d\varepsilon^{e} + d\varepsilon^{p} \tag{11.9}$$

where the prefix of "e" and the prefix of "p" designate elastic and plastic components, respectively. In the elastoplastic terminology, the elastic component is the one which is recovered upon removal of the loaded stress increments, while the plastic component remains unchanged (irreversible) upon unloading and reloading (Fig. 11.12). The elastic strain increments are calculated by a conventional elasticity framework. In a three-dimensional case, the isotropic theory of elasticity states

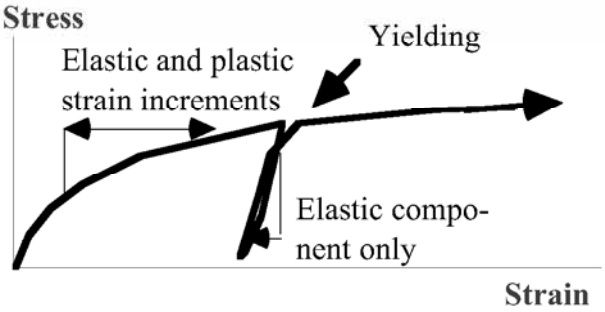

Fig. 11.12 Definition of elastic and plastic strain components

$$\begin{Bmatrix} d\varepsilon_{xx} \\ d\varepsilon_{yy} \\ d\varepsilon_{zz} \\ d\gamma_{xy} \\ d\gamma_{yz} \\ d\gamma_{zx} \end{Bmatrix}^{e} = \frac{1}{E} \begin{bmatrix} 1 & -\nu & -\nu & 0 & 0 & 0 \\ -\nu & 1 & -\nu & 0 & 0 & 0 \\ -\nu & -\nu & 1 & 0 & 0 & 0 \\ 0 & 0 & 0 & 2(1+\nu) & 0 & 0 \\ 0 & 0 & 0 & 0 & 2(1+\nu) & 0 \\ 0 & 0 & 0 & 0 & 0 & 2(1+\nu) \end{bmatrix} \begin{Bmatrix} d\sigma_{xx} \\ d\sigma_{yy} \\ d\sigma_{zz} \\ d\tau_{xy} \\ d\tau_{yz} \\ d\tau_{zx} \end{Bmatrix}^{e} \tag{11.10}$$

in which E is the Young's modulus (modulus of elasticity), ν is the Poisson ratio, and $E/\{2(1+\nu)\}$ is often called the shear modulus, G. In case that stress–strain relationship is nonlinear, these soil parameters are defined by tangent values and change with the magnitudes of stress components, void ratio, and possibly other soil parameters.

The theory of plasticity prefers to use the tensor way of designation for stress and strain. The relationships between the tensor designation and the engineering designation (11.10) are given by

$$\{\varepsilon_{11} \quad \varepsilon_{22} \quad \varepsilon_{33} \quad \varepsilon_{12} \quad \varepsilon_{21} \quad \varepsilon_{23} \quad \varepsilon_{32} \quad \varepsilon_{31} \quad \varepsilon_{13}\} = \{\varepsilon_{xx} \quad \varepsilon_{yy} \quad \varepsilon_{zz} \quad \gamma_{xy}/2 \quad \gamma_{xy}/2 \quad \gamma_{yz}/2 \quad \gamma_{yz}/2 \quad \gamma_{zx}/2 \quad \gamma_{zx}/2\}, \tag{11.11}$$

$$\{\sigma_{11} \quad \sigma_{22} \quad \sigma_{33} \quad \sigma_{12} \quad \sigma_{21} \quad \sigma_{23} \quad \sigma_{32} \quad \sigma_{31} \quad \sigma_{13}\} = \{\sigma_{xx} \quad \sigma_{yy} \quad \sigma_{zz} \quad \tau_{xy} \quad \tau_{xy} \quad \tau_{yz} \quad \tau_{yz} \quad \tau_{zx} \quad \tau_{zx}\}. \tag{11.12}$$

By using the tensor designations, the theory of plasticity (Hill, 1983) expresses increments of plastic strain as

$$d\varepsilon_{ij}^{p} = h\frac{\partial g}{\partial \sigma_{ij}}\, df \qquad (i,j = 1,2,3) \qquad (11.13)$$

in which h, g, and f are called hardening function, plastic potential, and yield function, which are functions of stress components and soil density possibly together with other soil parameters.

The theory of plasticity has several hypotheses. First, the plastic deformation occurs only when the yield function, f, increases. In other words, plastic deformation occurs only after yielding (Fig. 11.12) and no plastic deformation occurs when the current stress level is lower than the previous maximum value. In the extreme case where deformation is large close to failure, the yield function becomes similar to a failure criterion (Sect. 1.5).

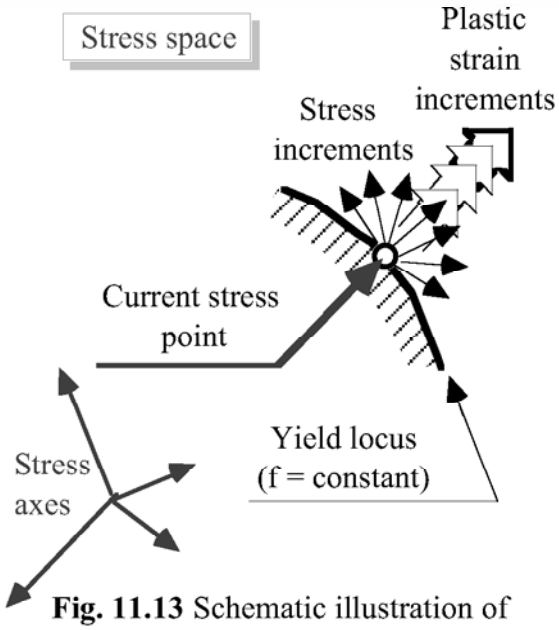

Fig. 11.13 Schematic illustration of plastic strain increments

Second, the ratio of components in a plastic strain increment (11.13) is independent of the magnitude and direction of stress increment. In other words, the orientation of the vector of plastic strain increment in Fig. 11.13 is independent of the direction and magnitude of the stress increment vector. This orientation is determined (flow rule) by partial derivative of the plastic potential function, $\partial g/\partial \sigma_{ij}$. Hence, this orientation is normal to the plane of constant g function. The stress–dilatancy relationship (Sect. 1.6) that is widely observed in soil testing determines the ratio of shear and volumetric strains and therefore is a kind of flow rule (Fig. 11.14).

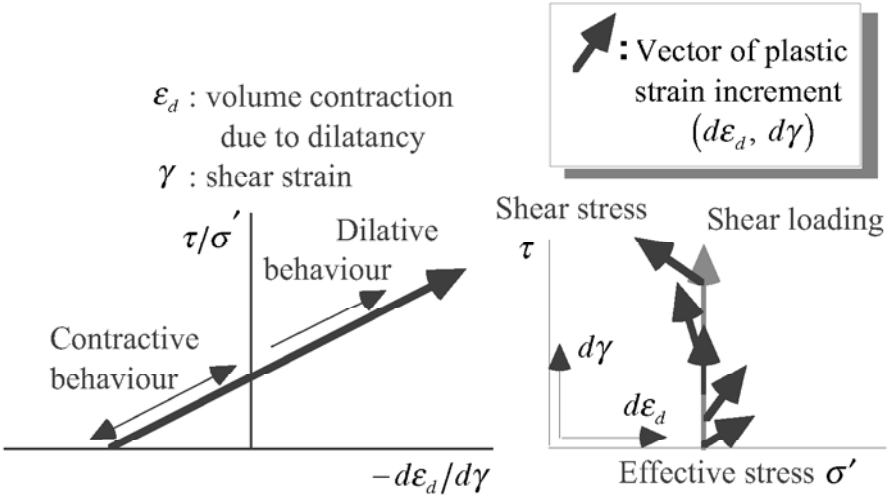

Fig. 11.14 Use of stress-dilatancy relationship as flow rule of plasticity

Some theories employ g that is equal to f (associated flow rule). In this situation, the vector of plastic strain increment is normal to the yield locus (Fig. 11.13). This feature is called normality. On the contrary, the nonassociated flow rule employs different f and g functions.

The magnitude of the plastic strain increment vector is determined by the increment of the yield function, $df = \left(\partial f/\partial \sigma_{ij}\right) d\sigma_{ij}$, in (11.13).

Principal stresses (Sect. 1.3) play a major role in plasticity theory. The requirement of objectivity states that the ground deformation as calculated by the plasticity theory has to be independent of the choice of coordinate directions (x-y-z system or x'-y'-z' system). Therefore, h, g, and f functions in (11.13) are functions of principal stresses that are independent of the coordinate system. In other words, they are functions of stress invariants such as

$\left(\sigma_1'+\sigma_2'+\sigma_3'\right)/3$, $\left(\sigma_1'-\sigma_2'\right)^2+\left(\sigma_2'-\sigma_3'\right)^2+\left(\sigma_3'-\sigma_1'\right)^2$, and $\sigma_1'\times\sigma_2'\times\sigma_3'$.

Effective stress components are used in the above expression because soil behavior is governed not by the total stress but by the effective stress. The third hypothesis of plasticity theory is called coaxiality, which states that the principal axes of stress and plastic strain increments are parallel to each other (Fig. 11.15).

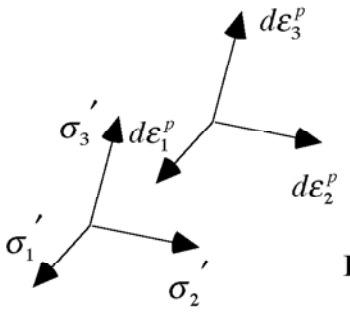

Fig. 11.15 Conceptual drawing of coaxiality

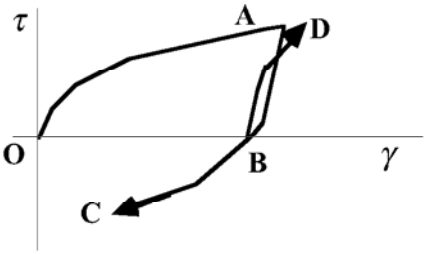

Fig. 11.16 Two variations of shear stress with different consequences

The use of principal stresses or stress invariants in functions *h*, *g*, and *f* causes one significant problem in application of plasticity theory to cyclic stress history. Figure 11.16 compares two kinds of shear stress history: OABC and OABD. Since the principal stress formulation cannot recognize the different direction of shear stress after B, continued soft behavior in BC and elastic reloading in BD cannot be reproduced. This problem is significant in the popular *P'-q* formulation $\left[P'=\left(\sigma_1'+\sigma_2'+\sigma_3'\right)/3 \text{ and } q=\sigma_1'-\sigma_3'\right]$ as well.

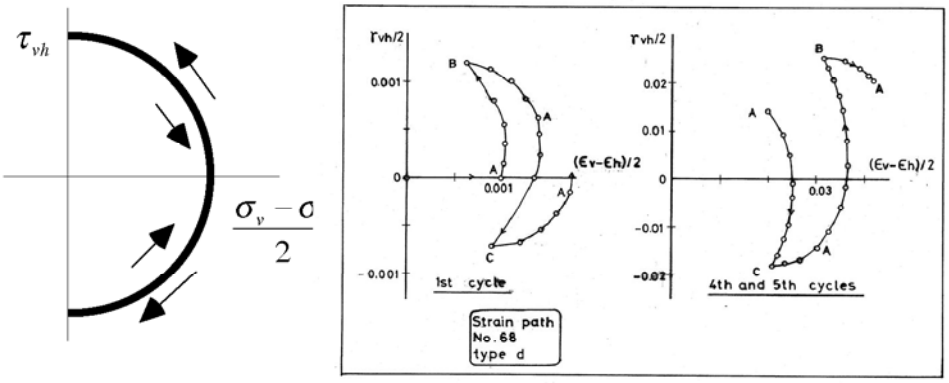

Fig. 11.17 Development of plastic shear strain under continuous rotation of principal stress axes

It is physically possible that principal stress axes rotate significantly while maintaining the magnitudes of σ_1', σ_2', and σ_3' constant. Since *f*, *g*, and *h* functions are held constant under constant values of principal stresses, the theory of plasticity does not give plastic stress increments; d*f* = *0* in (11.13). In reality, on the contrary, such stress components as τ_{xz} can still vary, and changes corresponding strain components (γ_{xz} for example). Consequently, plastic strain of γ_{xz}^{p} can develop (Ishihara and Towhata, 1983). Figure 11.17 illustrates the development of shear strains, $\left(\varepsilon_v-\varepsilon_h\right)/2$ and γ_{vh}, undergoing cyclic rotation of principal stress axes while maintaining $\sigma_1-\sigma_3$ constant. Figure 11.18 shows vectors of strain increments along another circular stress path. As the stress state approached failure in the third cycle, the vector became greater and more perpendicular to the circular stress path. Thus, the strain increment vector became overwhelmed by plastic components that were coaxial with the principal stress.

Consequently, it is reasonable to state that elastoplasticity theory for, in particular, complex cyclic loading should be formulated with special provisions for stress axes rotation; simple use of stress invariants is not appropriate. An example of such a provision is the use of stress difference tensor, $\sigma_{ij}-\sigma_{ij}^{*}$, in which σ_{ij}^{*} stands for the stress state at the beginning of unloading (Point A in Fig.

11.16). This kind of modeling produces plasticity mechanism even when the stress level decreases from the previous maximum value (inside the yield locus in the classical sense) as schematically illustrated in Fig. 11.19. Mroz et al. (1978) developed such a theory.

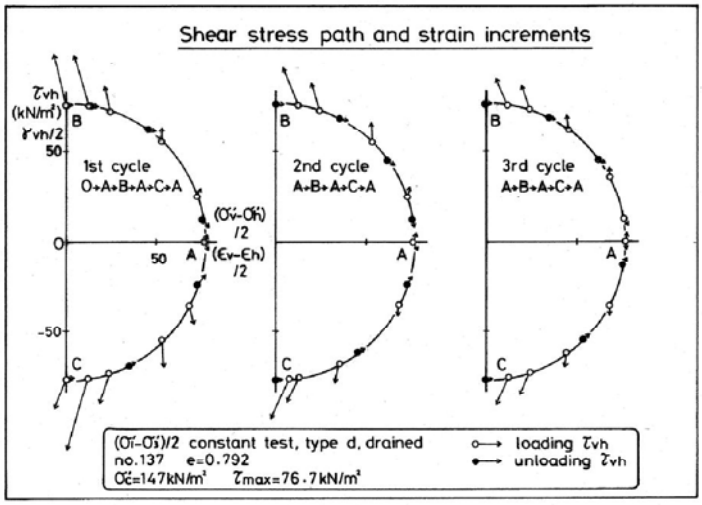

Fig. 11.18 Development of strain increments during continuous rotation of principal stress axes

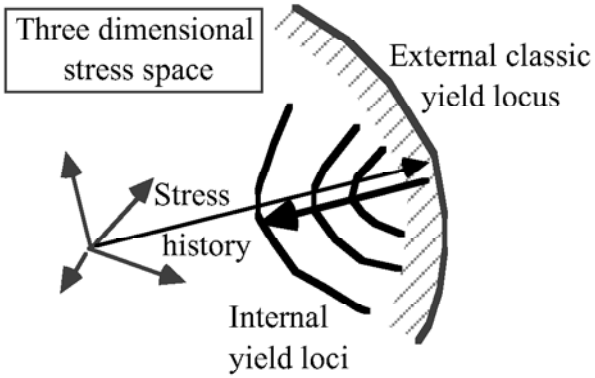

Fig. 11.19 Idea of multiple yield mechanisms of plasticity

Dilatancy is a phenomenon of volume change caused by shear deformation of discrete material (Sects. 1.2 and 1.6). In earthquake engineering practice, volume contraction due to dilatancy (negative dilatancy) is important because it stands for ground subsidence induced by strong shaking. Dilatancy plays an extremely important role in liquefaction analysis (Chap. 2) as well, because the major cause of liquefaction and large ground deformation is the development of high pore water pressure caused by dilatancy (Sect. 18.1).

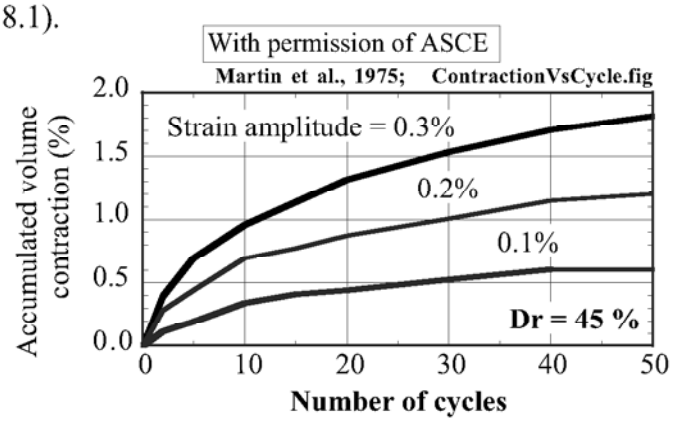

Fig. 11.20 Volume contraction of sand due to cyclic shear (Martin et al., 1975)

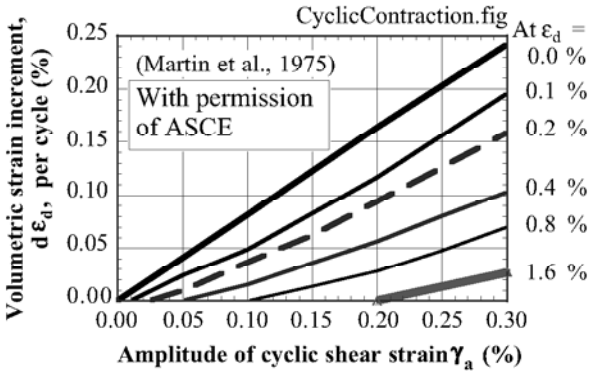

Fig. 11.21 Increment of volumetric strain per cycle of shear strain (Martin et al., 1975)

This section concerns modeling of dilatancy under one-dimensional cyclic shear loading. There are two kinds of approach for modeling of dilatancy. One is modeling of volume change, which is measured in cyclic drained shear of sand. Martin et al. (1975) conducted drained cyclic simple shear tests and reported that the volumetric strain due to dilatancy is proportional to shear strain amplitude; see Fig. 11.20. They studied the increment of volumetric strain per cycle (Fig. 11.21) and proposed an empirical formula,

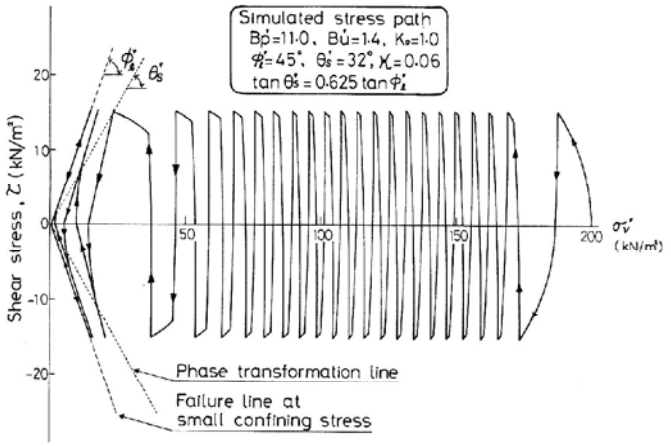

Fig. 11.22 Stress-path model of dilatancy and excess pore water pressure (see Set. 22.4)

$$d\varepsilon_d = C_1\left(\gamma_a - C_2\varepsilon_d\right) + \frac{C_3{\varepsilon_d}^2}{\gamma_a + C_4\varepsilon_d}, \quad (11.14)$$

where $d\varepsilon_d$ is the increment of volumetric strain per cycle of strain amplitude γ_a. If cyclic loading occurs in a drained manner (dry sand for example), this ε_d is equal to the real volume compression. If loading is undrained as is the case of liquefaction, this potential volume contraction is converted to the decrease in effective stress under constant volume by

$$d\sigma' = K\left(d\varepsilon_v - d\varepsilon_d\right), \quad (11.15)$$

where ε_v is the volumetric strain that does occur in reality. Note that $\varepsilon_v = 0$ under perfectly undrained conditions. Moreover, K is called bulk modulus of soil and is equivalent with $1/m_v$ (m_v being volume compressibility in (1.12)) in consolidation theory. The determination of soil parameters in (11.14) requires cyclic drained loading on undisturbed soil specimens.

The other approach to modeling of dilatancy is that of excess pore water pressure that develops during

undrained cyclic loading. Apparently, this approach is related with liquefaction tests on sand. Figure 11.22 (Ishihara and Towhata, 1982) indicates a modeled relationship between decrease in effective stress (increase in pore water pressure) and cyclic change in shear stress. This stress path model consists of three parts: under loading (increase of shear stress), unloading (decrease of shear stress), and that near perfect liquefaction.

Both approaches as described above concern one-dimensional cyclic loading (case of horizontal ground subjected to one direction, EW or NS, of shaking). For more complicated situations, those models have to be significantly revised, or more complicated models such as stress–dilatancy approach of plasticity (Sects. 1.6 and 11.3) for volume change or energy correlation of pore water pressure (Sect. 20.8–20.10) are employed.

Figure 11.23 illustrates an example of multi–nonlinear spring model for a two-dimensional situation in which simultaneous loading of $(\sigma_v - \sigma_h)/2$ and τ_{vh} associated with continuous rotation of principal stress axes is taken into account (Towhata and Ishihara, 1985). The big arrow in the figure stands for the above-mentioned shear stress components and its variation induces the displacement of the point of action at the center. This displacement stands for the shear strain of soil; $(\varepsilon_v - \varepsilon_h)/2$ and $\gamma_{vh}/2$. Note that the ratio of two stress components (direction of the arrow) indicates the orientation of principal stresses. When this orientation rotates, the direction of the arrow changes and component springs are subjected to nonlinear deformation. Consequently, plastic deformation is produced. This model was combined with the energy correlation of excess pore water pressure (Sects. 20.8–20.10) to reproduce the undrained cyclic behavior of loose sand. It was applied by Iai et al. (1992a,b) to develop a seismic design code of harbor structures.

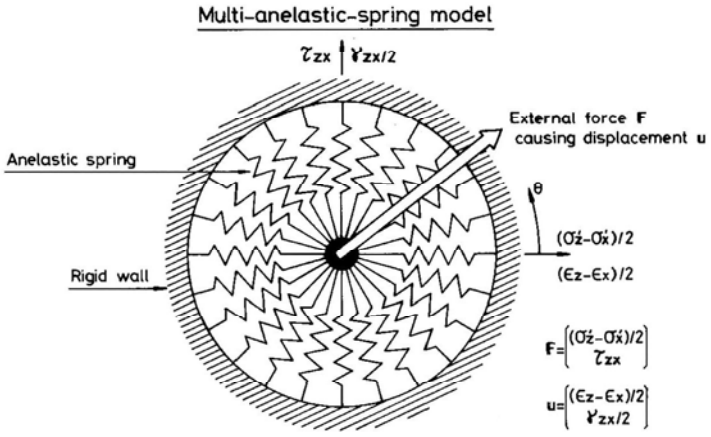

Fig. 11.23 Multi-spring model for two-dimensional shear deformation

The relationship between the nature of springs and the reproduced soil properties are as what follows. In an ideal case where the number of springs is infinite, the shear modulus of soil at small strain, G_{max}, and the spring modulus at small deformation, $k_{max}\mathrm{d}\theta$, are related to each other by supposing a loading in the direction of $\pi/2$ in Fig. 11.23;

$$G_{max} = \int_{\pi/2}^{5\pi/2} k_{max} \left\{ \cos\left(\theta - \frac{\pi}{2} \right) \right\}^2 \mathrm{d}\theta = \pi k_{max}. \qquad (11.16)$$

When the deformation of springs is extremely large, all the springs develop their full strength; $F_f\,\mathrm{d}\theta$. Accordingly, the magnitude of shear strength of modeled soil is given by

$$\text{Shear strength of soil} = 2\int_0^{\pi} F_f \cos\left(\theta - \frac{\pi}{2} \right) d\theta = 4F_f. \qquad (11.17)$$

These simple calculations assumed that all the springs have identical properties of k_{max} and F_f. By changing these parameters with the direction of springs, θ, it is possible to model anisotropic soil properties.

Since a two-dimensional condition has two independent shear stress components such as $(\varepsilon_z - \varepsilon_x)/2$ and γ_{zx} or γ_x and γ_y, the two-dimensional model illustrated in Fig. 11.23 is useful. In a three-dimensional condition, there are five independent shear stresses (six stresses minus mean effective stress) and its modeling by a multi-spring model is not easy. Simple expansion of the circle in the figure to a three-dimensional sphere is not sufficient because a sphere can handle only three degrees of freedom. Nishimura and Towhata (2004) solved this problem by allocating many circle models on the surface of a sphere; two degrees of freedom from a circle and three more degrees from the sphere.

It seems promising to extend the stress–dilatancy relationship (Fig. 11.14) to a multi-dimensional conditions. This goal may be achieved by employing the generalized shear stress of $\tau \equiv$

$\sqrt{\frac{3}{2}\left(\sigma'_{ij}-\delta_{ij}\sigma'_{\mathrm{m}}\right)\left(\sigma'_{ij}-\delta_{ij}\sigma'_{\mathrm{m}}\right)}$ and the generalized shear strain of $\gamma \equiv \sqrt{\frac{2}{3}\left(\varepsilon_{ij}-\frac{\delta_{ij}\varepsilon_{\mathrm{v}}}{3}\right)\left(\varepsilon_{ij}-\frac{\delta_{ij}\varepsilon_{\mathrm{v}}}{3}\right)}$. In these expressions, *i* and *j* are 1, 2, or 3, while δ_{ij} stands for the Kronecker´s delta;

$\delta_{ij} = 1$ if $i = j$ and $\delta_{ij}=0$ if $i \neq j$.

Moreover, $\sigma'_{\mathrm{m}} \equiv \left(\sigma'_1+\sigma'_2+\sigma'_3\right)/3$ designates the effective mean principal stress, and ε_{v} is the volumetric strain. Note that the above definitions of τ and γ follow the tensor abbreviation;

$A_k B_k \equiv \sum_k A_k B_k$ and, in particular, $\tau_{ij}\tau_{ij} \equiv \sum_i \sum_j \tau_{ij}\tau_{ij}$

The problem lying in the stress–dilatancy formulation is that no volumetric strain occurs if cyclic loading occurs with a constant value of γ; if $\mathrm{d}\gamma = 0$, $\mathrm{d}\varepsilon_{\mathrm{v}}$ has to be zero in order to avoid an infinite value of $\mathrm{d}\varepsilon_{\mathrm{v}}/\mathrm{d}\gamma$.

The bowl model was proposed by Fukutake and Matsuoka (1989) with a scope to predict volume contraction of sand undergoing multi-dimensional cyclic shear. For illustration, this section studies a situation of Fig. 11.24 where soil is sheared by two components of shear stress: τ_x and τ_y. The associating shear strains, γ_x and γ_y, are substituted in the dilatancy model in Fig. 11.25 where a bowl-like curved surface stands for the relationship between volume change and shear strain. The concave shape stands for the fact that volume expands when shear strain is large. See its similarity with the experimental curve in Fig. 11.8.

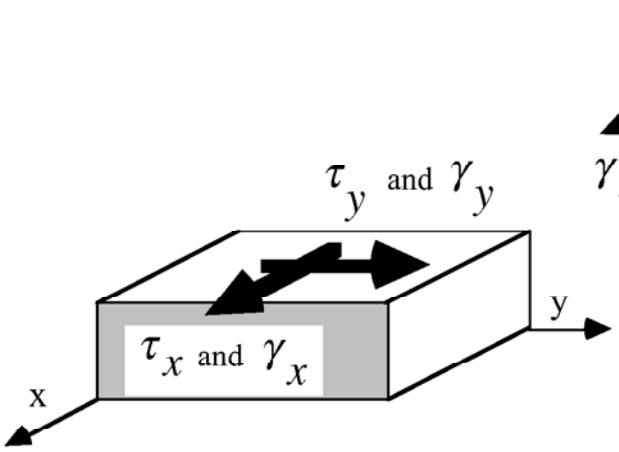

Fig. 11.24 Soil subjected to two-dimensional shear

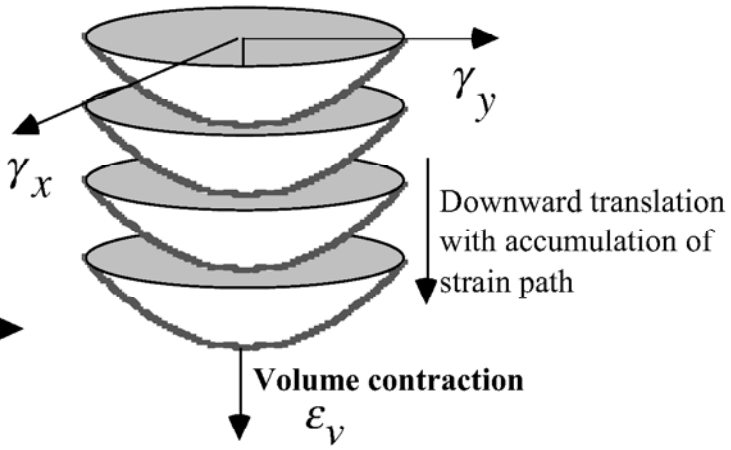

Fig. 11.25 Conceptual illustration of bowl model of dilatancy

Since the volume of soil further continues to contract with the number of shear cycles, the bowl surface moves down in Fig. 11.25, thus representing the accumulated volumetric contraction during cyclic loading. This downward translation is a function of the shear strain path;

Length of shear strain path $\equiv \int\left[\left(\mathrm{d}\gamma_x\right)^2+\left(\mathrm{d}\gamma_y\right)^2\right]$.

11.6 Discrete Element Analysis

Although the finite element analysis has been proved to be a powerful tool to calculate deformation of a continuous medium, there have been different attempts that consider materials discontinuous. This attempt is appropriate for such situations as post-failure behavior of rock slopes in which blocks of breached rock move and collide independently (Cundall, 1971; Kawai and Takeuchi, 1981).

Deformation analysis on an assembly of circular or spherical objects started in 1950s (Deresievicz, 1958a,b). Since sand consists of grains, this approach is attractive; particularly being so when displacement is large. Hence, a method of analysis called distinct element analysis or discrete element analysis (DEM) has been developed in which particles move and collide with each other (Cundall and Strack, 1979). However, the limited capacity of computers has not allowed to analyze behavior of real individual grains in either two-dimensional or three-dimensional manners; the number of real grains is too many for any computer memory. Hence, the existing DEM works in a two-dimensional manner on imaginary grains, which are much bigger than real grains. The two-dimensional analysis employs void ratio, which is smaller than the well-known void ratio range in real sandy deposit. For example, a regular packing of round grains in Fig. 11.26 has void ratio of $1-\pi/4 = 0.273$.

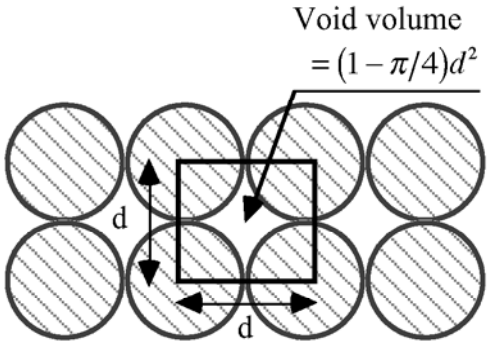

Fig. 11.26 Regular packing of two-dimensional circular grains

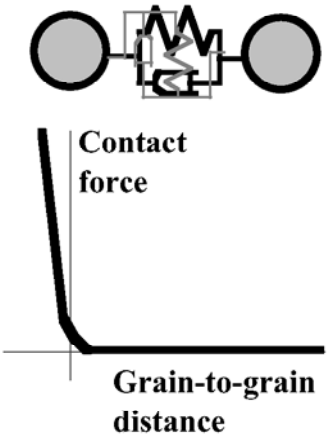

Fig. 11.27 Contact mechanism in normal direction

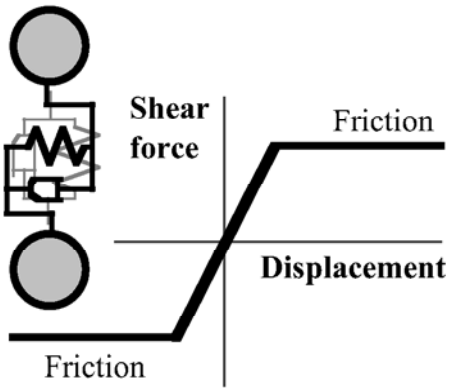

Fig. 11.28 Contact mechanism in shear direction

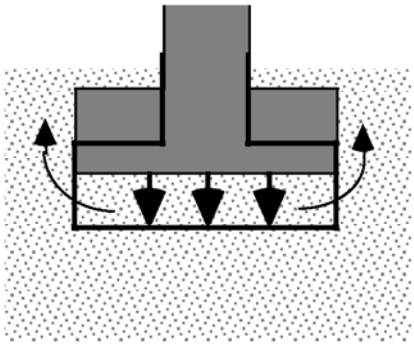

Fig. 11.29 Grains turning around corner

In DEM, the grain-to-grain interaction is modeled by nonlinear springs and dashpots, which are illustrated in Figs. 11.27 and 11.28. When the grain-to-grain distance is short, a particle contact occurs, and a normal mechanism (Fig. 11.27) is activated to resist against compression. At the same time, a shear resistant mechanism (Fig. 11.28) is generated that stands for friction between grains. The magnitude of friction in Fig. 11.28 varies with the extent of contact force in Fig. 11.27. DEM analysis is more advantageous than FEM when displacement and deformation are large. For example, DEM can calculate grain movements that turn around a corner of sinking foundation (Fig. 11.29), while such an analysis is very difficult in FEM.

In a dynamic analysis, the grain-to-grain distance has to be examined for pairs of extremely many particles at every time increment. To make ease this procedure, most DEM analyses employ circular or spherical grains. Moreover, previous DEM assumed only such two types of mechanisms as compression and shear at contact points. This idea is reasonable when the real contact occurs at a single point. If the real contact occurs by a plane or two points, the transfer of moment becomes important. Iwashita and Oda (1998) installed bending moment mechanism at contacts of imaginary spherical particles.

For an application to geotechnical earthquake problems, Kanatani et al. (2001) combined FEM and DEM in which FEM was applied to a more continuous soil deposit, while DEM to an accumulation of big concrete pieces. Furthermore, Hakuno and Tarumi (1988) as well as Nakase et al. (1998) showed how to calculate excess pore water pressure and seepage flow in a water-saturated model. Figure 11.30 illustrates an example calculation of liquefaction-induced deformation in a 30*g* centrifuge test. The number of spherical elements are 14,000 with the diameter of 0.4 mm. Shaking of 300 Gal with 2 Hz was applied. It is seen in this figure that the subsidence was terminated after some subsidence at which the buoyancy and gravity forces achieved equilibrium. Note that the force equilibrium after some displacement can be reproduced by FEM only if a large-displacement formulation is employed.

A three-dimensional DEM analysis is very interesting but evidently difficult because of the heavy computation load. Harada and Gotoh (2006) conducted this type of analysis on the transportation of river bed grains, taking simply into account the water effects. They employed 9,350 grains.

(a) Initial configuration prior to shaking.

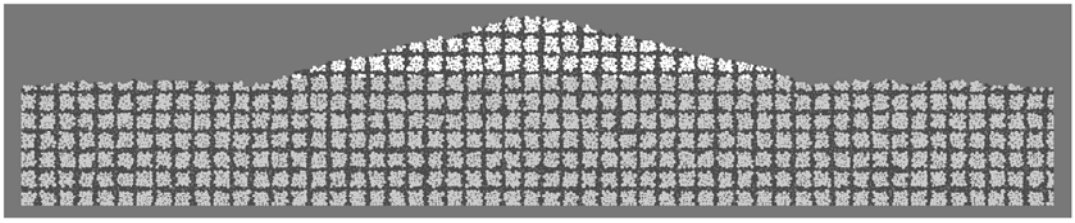

(b) Confguration after subsidence into liquefied subsoil.

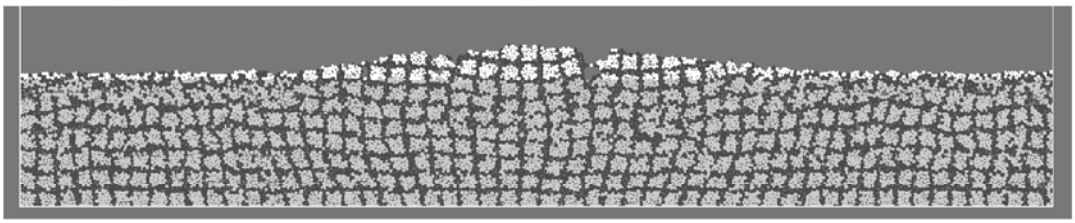

Fig. 11.30 DEM calculation on subsidence of embankment into liquefied subsoil (Honda and Towhata, 2006)

List of References in Chapter 11

Cundall, P.A. (1971) A computer model for simulating progressive, large-scale movements in blocky rock systems, Proc. Symp. Int. Soc. Rock Mech., Nancy, p. II-8.

Cundall, P.A. and Strack, O.D.L. (1979) A discrete numerical model for granular assemblies, Geotech., Vol. 29, No. 1, pp. 47–65.

Deresiewicz, H. (1958a) Mechanics of granular matter, Advances in Applied Mechanics, Academic Press, New York, pp. 233–306.

Deresiewicz, H. (1958b) Stress–strain relations for a simple model of a granular medium, J. Appl. Mech., Vol. 25, pp. 402–406.

Fukutake, K. and Matsuoka, H. (1989) A unified law for dilatancy under multi-directional simple shearing, Proc. JSCE, No. 412/III-12, pp. 240–248 (in Japanese).

Hakuno, M. and Tarumi, Y. (1988) A granular assembly simulation for the seismic liquefaction, Struct. Eng. / Earthq. Eng., Vol. 5, No. 2 (Proc. JSCE, No.398/I-10), pp. 333–342.

Harada, E. and Gotoh, H. (2006) Numerical simulation of sediment sorting in sheetflow regime by 3D granular material model, Proc. JSCE B, Vol. 62, No. 1, pp. 128–138 (in Japanese).

Hardin, B.O. and Drnevich, V.P. (1972) Shear modulus and damping in soils design equation and curves, Proc. ASCE, Vol. 98, SM7, pp. 667–692.

Hill, R. (1983) The mathematical theory of plasticity, The Oxford Engineering Science Series, pp. 14–69 (first edition in 1950).

Hinokio, M., Nakai, T., Hoshikawa, T. and Yoshida, H. (2001) Dilatancy characteristics and anisotropy

of sand under monotonic and cyclic loading, Soils Found., Vol. 41, No. 3, pp. 107-124.
Honda, T. and Towhata, I. (2006) Factors influencing ground deformation of river dike due to liquefaction by distinct element analysis, Proceedings of IS-Yamaguchi 06 on Geomechanics and Geotechniques of Particulate Media, Ube, Yamaguchi, Japan, pp. 225–232.
Iai, S., Matsunaga, Y. and Kameoka, T. (1992a) Strain space plasticity model for cyclic mobility, Soils Found., Vol. 32, No. 2, pp. 1–15.
Iai, S., Matsunaga, Y. and Kameoka, T. (1992b) Analysis of undrained cyclic behavior of sand under anisotropic consolidation, Soils Found., Vol. 32, No. 2, pp. 16–20.
Ishihara, K. and Towhata, I. (1982) Dynamic response analysis of level ground based on the effective stress method, Soil Mechanics – Transient and Cyclic Loads, Wiley, New York, pp. 133–172.
Ishihara, K. and Towhata, I. (1983) Sand response to cyclic rotation of principal stress directions as induced by wave loads, Soils Found., Vol. 23, No. 4, pp. 11–26.
Iwashita, K. and Oda, M. (1998) Rolling resistance at contacts in simulation of shear band development by DEM, J. Eng. Mech., ASCE, Vol. 124, No. 3, pp. 285–292.
Jennings, P.C. (1964) Periodic response of a general yielding structure, Proc. ASCE, Vol. 90, EM2, pp. 131–166.
Kanatani, M., Kawai, T. and Tochigi, H. (2001) Prediction method on deformation behavior of caisson-type seawalls covered with armored embankment on man-made islands during earthquakes, Soils Found., Vol. 41, No. 6, pp. 79–96.
Kawai, T. and Takeuchi, N. (1981) A discrete method of limit analysis with simplified elements, Proc. 1st Int. Conf. Computing in Civil Eng., pp. 27–42.
Kondner, R.L. (1963) A hyperbolic stress–strain response: Cohesive soils, Proc. ASCE, Vol. 89, SM1, pp. 115–143.
Kondner, R.L. and Zelasko, J.S. (1963) A hyperbolic stress–strain formulation for sands, Proc. 2nd Pan-American Conf. Soil Mech. Found. Eng., Vol.I, pp. 289–324.
Martin, G.R., Finn, W.D.L. and Seed, H.B. (1975) Fundamental of liquefaction under cyclic loading, Proc. ASCE, Vol. 101, GT5, pp. 423–38.
Masing, G. (1926) Eigenspannungen und Verfestigung beim Messing, Proc. 2nd Int. Cong. Applied Mechanics, pp. 332–335.
Mroz, Z., Norris, V.A. and Zienkievicz, O.C. (1978) An anisotropic hardening model for soils and its application to cyclic loading, Int. J. Nume. Anal. Methods Geomech., Vol. 2, pp. 203–221.
Nakase, H. (1999) A simulation study on liquefaction using DEM, Mechanics of Granular Materials, an Introduction, ed. M. Oda and K. Iwashita, publ. A.A.Balkema, The Netherlands, pp. 183–187.
Nishimura, S. and Towhata, I. (2004) A three-dimensional stress–strain model of sand undergoing cyclic rotation of principal stress axes, Soils Found., Vol. 44, No. 2, pp. 103–116.
Pradhan, T.B.S., Tatsuoka, F. and Sato, Y. (1989) Experimental stress–dilatancy relations of sand subjected to cyclic loading, Soils Found., Vol.2 9, No. 1, pp. 45-64.
Shahnazari, H. and Towhata, I. (2002) Torsion shear tests on cyclic stress–dilatancy relationship of sand, Soils Found., Vol. 42, No. 1, pp. 105-119.
Towhata, I. and Ishihara, K. (1985) Modelling soil behaviour under principal stress axes rotation, Proc. of 5th International Conference on Numerical Methods in Geomechanics, Nagoya, Japan, Vol. 1, pp. 523–530.

Chapter 12

Application of Seismic Inertia Force

The five-storeyed Buddhism pagoda in Horyu-ji Temple (法隆寺), Nara, Japan. This temple, inclusive of this pagoda, was first constructed in A.D. 607. It is said that the original temple was destroyed by fire in 670 and reconstructed later. There is a recent archaeological finding that supports this story. Whether this story of fire is true or not, Horyu-ji is the world oldest wooden building.

12.1 Calculation of Earthquake-Induced Displacement

In the recent times, except those caused by soil liquefaction, there has been few failure of dam due to earthquakes. An important issue, therefore, is the prevention of unallowable deformation of a dam embankment. This need has led to a study on the residual displacement of a soil body that remains after the end of shaking.

Newmark (1965) proposed an analogy between the seismic slope movement and the motion of a rigid block on a frictional slope (Fig. 12.1). When the rigid block of mass "*m*" is subjected to a cyclic base acceleration parallel to the floor, an inertia force of *Kmg* is loaded on. Note that *K* is a function of time. Accordingly, (1) the block starts to move downwards when the exciting force plus the gravity effects exceed the frictional resistance, and (2) it decelerates its velocity when the friction exceeds the cyclic plus the gravity forces. The equation of motion of the rigid block is given by

$$\frac{\mathrm{d}^2 u}{\mathrm{d}t^2} = g(\sin\alpha + K - \mu\cos\alpha) = g(K - K_{\mathrm{cr}}) \qquad (12.1)$$

in which α is the slope angle and μ the frictional coefficient. Under a preearthquake static condition, the factor of safety is given by $F_s = \mu/\tan\alpha$. The downward motion starts when K exceeds $K_{\mathrm{cr}} = \mu\cos\alpha - \sin\alpha$. The upward motion is ignored for conservatism (安全側の考え方) in many practical studies, although it is possible to start when *negative K exceeds* $-(\mu\cos\alpha + \sin\alpha)$.

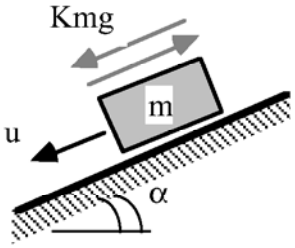

Fig. 12.1 Newmark´s analogy of sliding rigid block of frictional floor

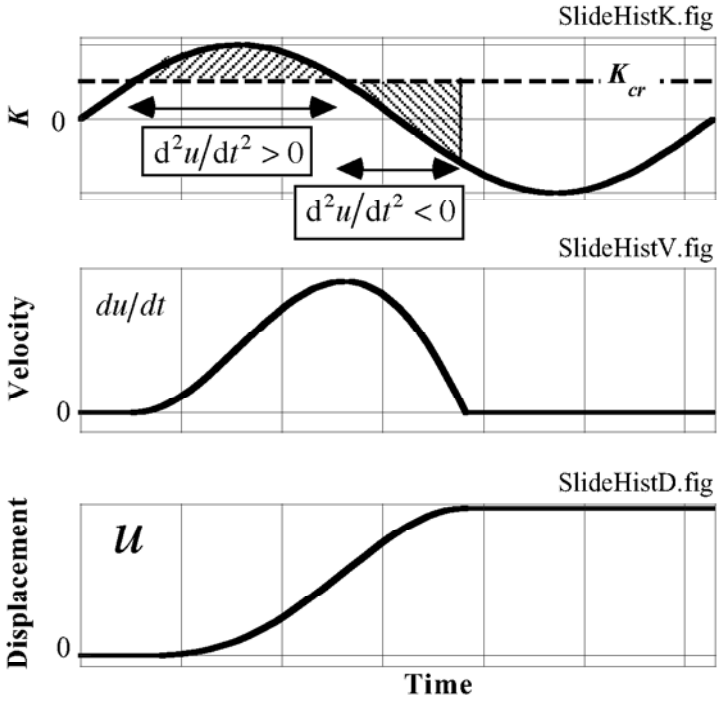

Fig. 12.2 Initiation and termination of sliding movement in Newmark analogy

Since the Newmark analogy relies on shear failure mechanism, no elastic component is taken into account. Figure 12.2 illustrates the initiation and termination of slip movement. First, the movement starts when K exceeds K_{cr}, making the acceleration greater than zero and velocity increases with time. This situation continues until K becomes less than K_{cr} after which $\mathrm{d}^2u/\mathrm{d}t^2$ becomes negative and velocity decreases. As shown in the time history of displacement, the displacement continues to increase without fluctuation and ceases to increase any more when the velocity becomes zero.

An example analysis is presented below by using a harmonic excitation;

$$K = K_{\max}\sin\omega t. \qquad (12.2)$$

Although this K is similar to the static inertia force employed in conventional seismic designs (Sect. 7.1), it is different in a sense that this K changes with time. Hence, K is equivalent with a base acceleration.

The motion starts at $t_0 = \arcsin(K_{cr}/K_{max})/\omega$ at which $K = K_{cr}$. By substituting (12.2) in (12.1) and integrating with time,

$$\frac{\omega}{gK_{cr}}\frac{du}{dt} = -\frac{K_{max}}{K_{cr}}\left(\cos\omega t - \cos\omega t_0\right) - \left(\omega t - \omega t_0\right). \qquad (12.3)$$

The end of sliding, $t = t_1$, is detected by making the right-hand side of (12.3) equal to zero (velocity = 0). The solution for this is obtained by Newtonian iterative method; $x_{i+1} = x_i - F(x_i)/\{dF(x_i)/dx\}$; with the initial assessment of $\omega t_1 = 1.5\pi$. Finally by integrating (12.3) once more with time from t_0 to t_1, the development of displacement per cycle, denoted by U_1, is calculated. See Fig. 12.3 for the duration time of sliding and Fig. 12.4 for U_1. Note that sliding starts early and lasts for a longer time when K_{max} value is greater. Consequently, the magnitude of sliding displacement is greater as well.

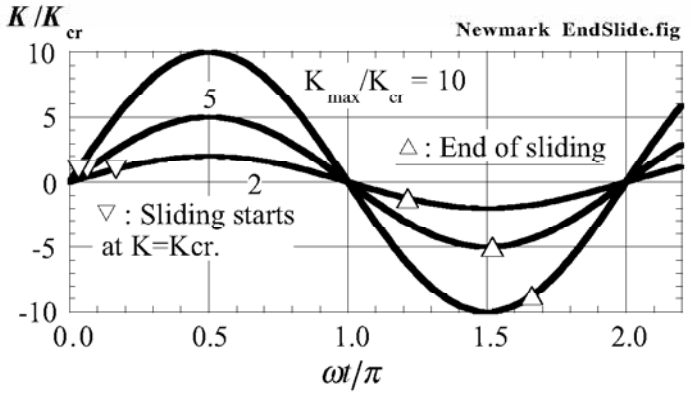

Fig. 12.3 Duration time of sliding under different intensity of inertia force

Exercise: Study the effects of shaking frequency on the residual displacement per cycle and per second by using Fig. 12.4 and Table 12.1.

A typical result is illustrated in Fig. 12.5 where frequency was varied 5 times over a range of the static factor of safety. Evidently, the higher shaking frequency causes significantly less magnitude of residual displacement. This implies that such an earthquake input motion with high acceleration but high frequency is not necessarily harmful to structures.

In practice, the rigid block in Fig. 12.1 is a replacement of a sliding soil mass, while the frictional floor is equivalent with a slip plane with $\mu = \tan\phi$.

Since the Newmark method was originally intended for a dam analysis, it basically concerns with a good compacted material. Therefore, it does not pay attention to excess pore water pressure development and the consequent loss of resistance.

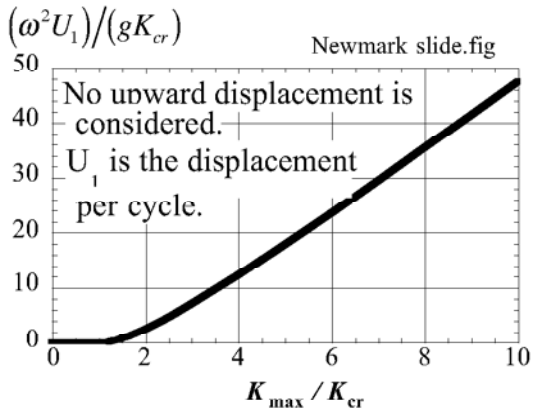

Fig. 12.4 Residual displacement per cycle predicted by Newmark analysis

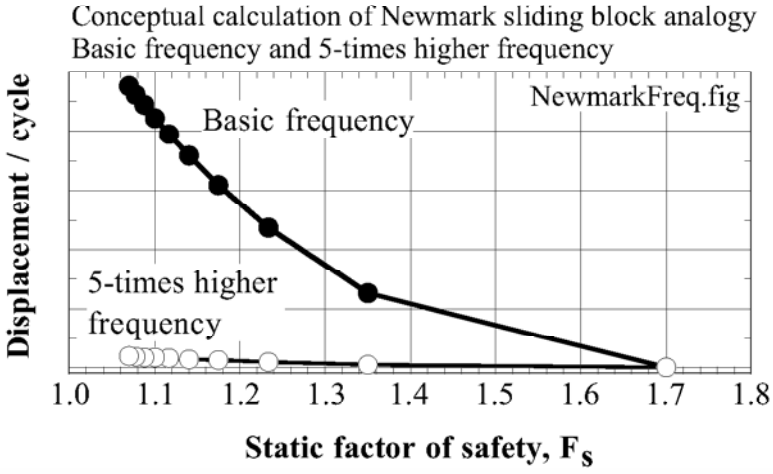

Fig. 12.5 Effects of shaking frequency on residual displacement as calculated by Newmark analogy

It should be recalled that one of the essences of geotechnical earthquake damage is the displacement which remains after an earthquake. This displacement is called the residual or permanent displacement. To study this aspect, the data in Fig. 12.4 is tabulated in Table 12.1.

Table 12.1 Relationship between intensity of dynamic inertia force and accumulation of residual displacement per cycle (see Fig. 12.2)

K_{max}/K_{cr}	$\omega^2 U_1/gK_{cr}$
1.0	0.00
2.0	2.53
3.0	7.11
4.0	12.36
5.0	17.94
6.0	23.70
7.0	29.57
8.0	35.52
9.0	41.53
10.0	47.57

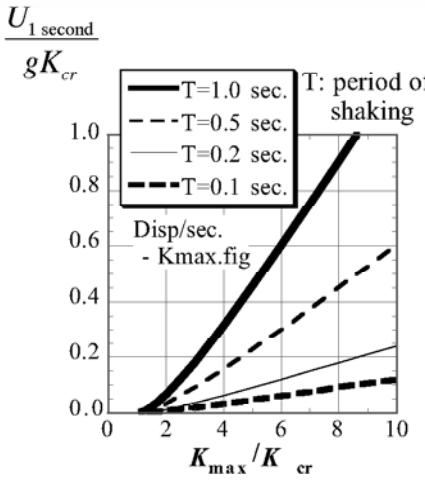

Fig. 12.6 Correlation between residual displacement and intensity of base acceleration

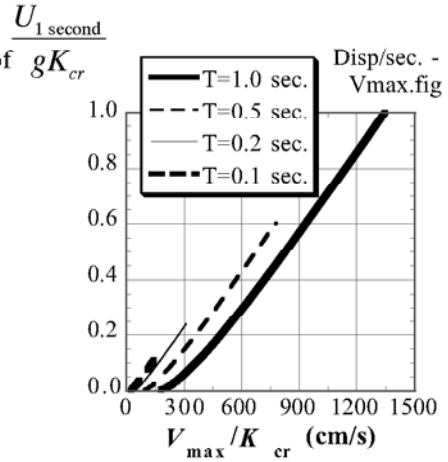

Fig. 12.7 Correlation between residual displacement and intensity of base velocity

Because U_1 above is a residual displacement per cycle, it does not carry much practical sense. It seems better to use the residual displacement per second, which is derived as $U_{1\,second} = U_1 \times$ frequency. In reality, what is reported as the residual displacement (of foundations and slopes) is equal to $U_1 \times$ frequency$\times$(Duration time of strong earthquake motion).

Figures 12.6 and 12.7 plot $U_{1\,second}/(gK_{cr})$ against the intensity of base acceleration (K_{max}; Fig. 12.6) and the amplitude of velocity at base ($V_{max} = gK_{max}/\omega$; Fig. 12.7). Although the residual displacement increases with these two typical earthquake motion parameters, there is not seen a good unique correlation. This is the reason why there is yet no agreement about the suitable earthquake intensity parameter to be used in practice.

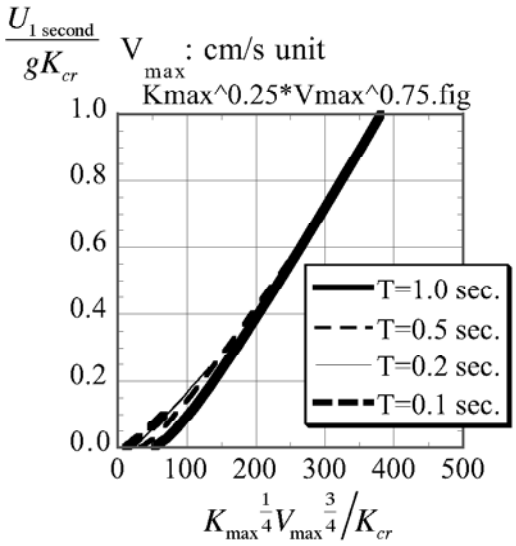

Fig. 12.8 Correlation between residual displacement and combined effects of base acceleration and velocity

Since the correlation in terms of velocity in Fig. 12.7 is more promising than that of K_{max}, it seems reasonable that seismic damage estimation is better carried out by velocity than the maximum acceleration. To further improve this, a new parameter of $K_{max}{}^{\frac{1}{4}} V_{max}{}^{\frac{3}{4}}$ was attempted in Fig. 12.8. Its correlation with the residual displacement per second appears reliable.

Ohmachi et al. (1990) proposed an idea of sliding response spectrum that indicates the power of a real earthquake motion to cause a sliding block displacement. The residual displacement after the whole earthquake changed with the slope angle and the frictional coefficient of the floor (α and μ in Sect. 12.1).

12.3 Relationship Between Seismic Coefficient and maximum Acceleration During Earthquakes

The seismic coefficient, K, that is applied in a static manner in design (Sect. 7.1) and the magnitude of acceleration, A_{max}, during earthquakes are not equivalent to each other in reality in spite of the d´Alembert principle. Surface acceleration with the maximum value of $A_{max} = 980 \times 0.7$ Gal is not so destructive as $K = 0.7$. This is because the duration of acceleration is limited and may not give structures time to move significantly, while the static seismic inertia force with $K = 0.7$ is hypothesized to last forever in design.

Noda et al. (1975) analyzed past earthquake damages in quay walls at harbors. Limit equilibrium analyses with a static seismic inertia force gave the critical K values, denoted as K_{cr}, which were required to induce failure. The real values of K was probably greater than K_{cr} at sites with damage, while K was less than K_{cr} when there was no damage. Thus, a range of possible K values were obtained.

At the same time, they estimated the maximum horizontal acceleration, A_{max}, by using the acceleration records obtained at nearby sites, or by using fault models, attenuation with the epicentral distance, and response analysis on local subsoil models.

By combining these all, the range of realistic K was plotted against A_{max} (Fig. 12.9). An empirical formula of $K = (A_{max}/g)^{1/3}/3$ was proposed. Figure 12.9 was a unique attempt to physically correlate K and A_{max}. Note that there are many uncertainties in this study, probably including the determination of appropriate soil strength in the limit equilibrium analysis.

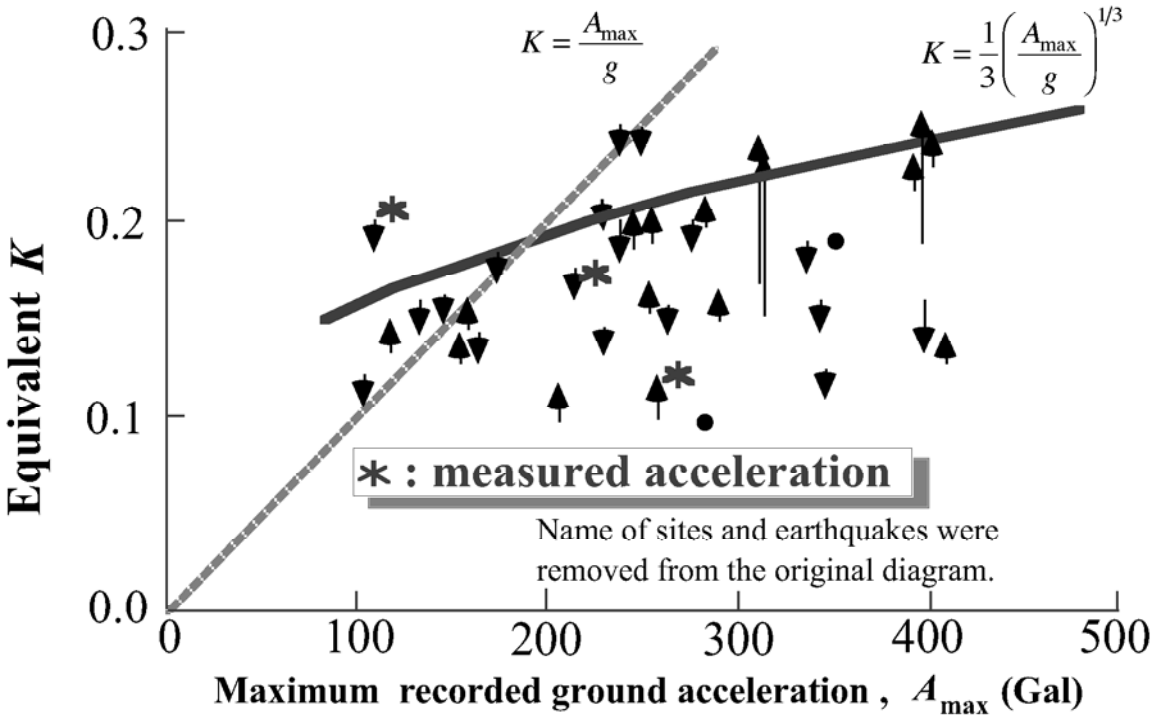

Fig. 12.9 Correlation between maximum acceleration and seismic coefficient (drawn after Noda et al. 1975)

12.4 Brief Analysis on Seismic Coefficient Equivalent to Maximum Acceleration

An attempt was made to determine the pseudo-static seismic coefficient that is equivalent with a given seismic loading. Figure 12.10 shows a simple time history of acceleration in which the wave shape is rectangular with a period of T and the amplitude equal to A_{max}. When a rigid mass resting on a level frictional floor (Fig. 12.11) is subjected to this acceleration history, the equation of motion is given by

$$m\frac{\mathrm{d}^2u}{\mathrm{d}t^2} = mA_{max} - \mu mg \quad \text{for } 0 \le t \le \frac{T}{2}$$
$$m\frac{\mathrm{d}^2u}{\mathrm{d}t^2} = -mA_{max} - \mu mg \quad \text{for } \frac{T}{2} \le t \le T,$$

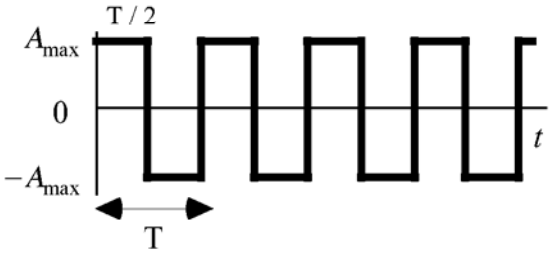

Fig. 12.10 Rectangular history of acceleration

which is easily integrated with the initial conditions of $u = \mathrm{d}u/\mathrm{d}t = 0$ at $t = 0$. Consequently, it is found that the motion stops at $t = A_{max}T/(A_{max} + \mu g)$ in which g stands for the gravitational acceleration. By assuming that the mass does not move back towards the original position after this time, the residual displacement per one cycle of shaking is derived;

$$u_{/\text{cycle}} = \frac{A_{max}T^2(A_{max} - \mu g)}{4(A_{max} + \mu g)}.$$

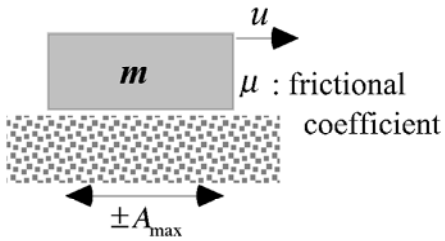

Fig. 12.11 Rigid mass resting on frictional level floor, which is subjected to motion

When the hypothetical earthquake has N cycles of shaking, the ultimate residual displacement at the time of NT is derived as

$$u_{ult} = \frac{NA_{max}T^2(A_{max} - \mu g)}{4(A_{max} + \mu g)}. \qquad (12.4)$$

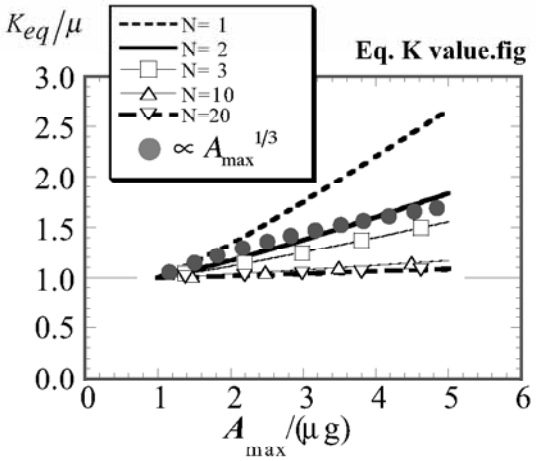

Fig. 12.12 Equivalent seismic coefficient

Second, a static seismic force of Kmg is applied to the mass in Fig. 12.11. By integrating the equation of motion with this constant (pseudostatic) force, the residual displacement, $u_{inertia}$, at $t = NT$ is easily derived as

$$u_{inertia} = \frac{(K - \mu)g(NT)^2}{2}. \qquad (12.5)$$

By equating (12.4) and (12.5), a value of $K = K_{eq}$ that is equivalent with the acceleration in Fig. 12.10 is determined;

$$\frac{K_{eq}}{\mu} = 1 + \frac{\frac{A_{max}}{\mu g}\left(\frac{A_{max}}{\mu g} - 1\right)}{2N\left(\frac{A_{max}}{\mu g} + 1\right)}. \qquad (12.6)$$

> K_{eq} here is equivalent with the given acceleration history in the sense that both develops the same magnitude of residual displacement after the same time.

Figure 12.12 plots K_{eq} thus calculated against $A_{max}/\mu g$. Note that K_{eq} decreases as N increases. The proportionality to $(A_{max}/g)^{1/3}$ as proposed by Noda et al. (1975) (Sect. 12.3) agrees with the case of $N = 2$. When more than two cycles occur, even a smaller K_{eq} is appropriate.

Calculation of seismic earth pressure on a retaining wall is one of the important applications of the pseudo-static (quasi-static) seismic inertial force. Figure 12.13 indicates the real failure of a wall. Not only lateral sliding but also rotation occurs in reality.

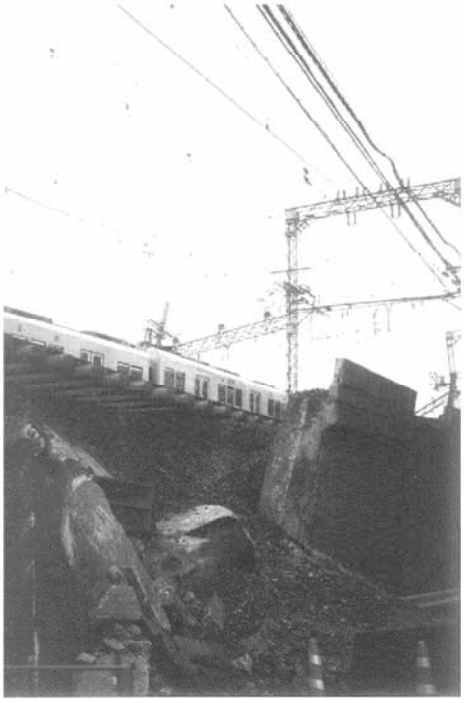

Fig. 12.13 Overturning of retaining wall during 1995 Kobe earthquake (near Hanshin Ishiyagawa Station)

Fig. 12.14 Prof. N.Mononobe around 1930

Fig. 12.15 Dr. S.Okabe in 1926

Mononobe and Okabe (Figs. 12.14 and 12.15) developed a theory of seismic earth pressure by modifying the Coulomb theory on (static) active earth pressure (Mononobe, 1924, Okabe, 1924, 1929; Mononobe and Matsuo, 1929). The Mononobe-Okabe theory is still in practical use all over the world.

Mononobe-Okabe pressure is a pressure at limit equilibrium. Do not confuse it with the real earth pressure during earthquake but without failure.

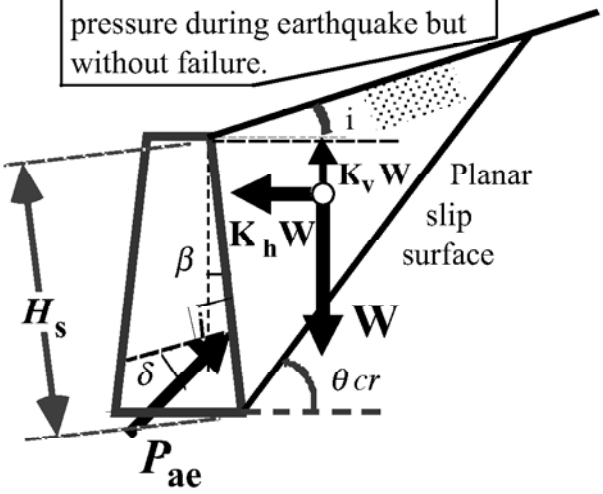

Fig. 12.16 Failure mechanism assumed in Mononobe–Okabe formula

Figure 12.16 illustrates the situation in which Mononobe–Okabe theory was developed. A soil wedge (楔くさび) behind a rigid wall is subjected to inertial forces in both horizontal and vertical directions. Since an active pressure is going to be studied, the horizontal inertia force is oriented outwards. The rear face of the wall is inclined by β, having a frictional angle of δ with soil.

The gravity force, W, is a static force that is oriented vertically and acting on the soil wedge. Under seismic conditions, inertia forces of $K_v W$ and $K_h W$ are added to W, composing a total load of W^*, which is inclined by ψ (Fig. 12.17).

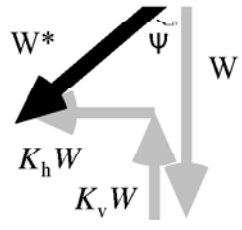

$$\Psi = \arctan\frac{K_h}{1 - K_v}$$

Fig. 12.17 Total force acting on soil wedge

By examining Figs. 12.16 and 12.17, it is found that Mononobe–Okabe theory is different from Coulomb's active-earth-pressure theory (Fig. 12.18) only in the direction of force W^*. Hence, the Mononobe–Okabe's Fig. 12.16 is rotated by ψ to obtain Fig. 12.19 where the force of W^* is vertical. By applying the original Coulomb theory to Fig. 12.19, the seismic

active earth pressure, P_{ae}*, is derived.

The original Coulomb active pressure was given by

$$P_a = \frac{\gamma H_s^2}{2} \frac{\cos^2(\phi-\beta)}{\cos(\delta+\beta)\left\{1+\sqrt{\dfrac{\sin(\phi+\delta)\sin(\phi-i)}{\cos(\delta+\beta)\cos(i-\beta)}}\right\}^2} \qquad (12.7)$$

and the direction of the slip plane by

$$\cot(\theta_{cr}-i) = -\tan(\beta-i+\delta+\phi) + \frac{1}{\cos(\beta-i+\delta+\phi)}\sqrt{\frac{\sin(\phi+\delta)\cos(\beta+\delta)}{\cos(\beta-i)\sin(\phi-i)}}, \qquad (12.8)$$

where H_s is the length of the face of the wall. For detailed derivation of (12.7) and (12.8), refer to Appendix 1.

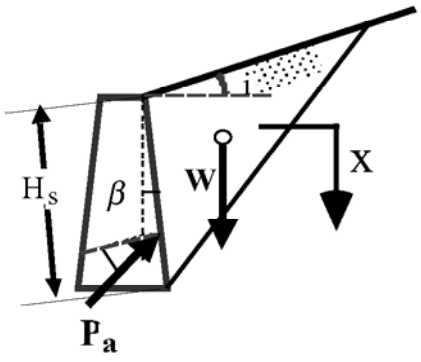

Fig. 12.18 Coulomb coordinate before rotation

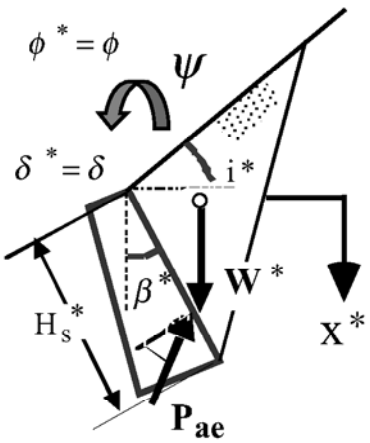

Fig. 12.19 Mononobe–Okabe coordinate after rotation

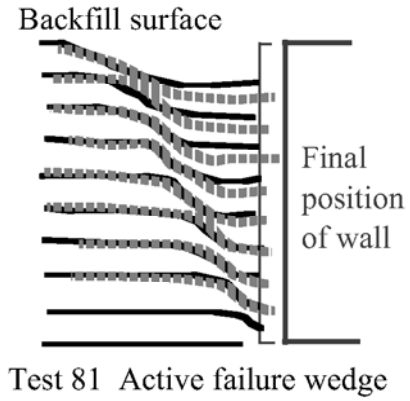

Fig. 12.20 Displacement of backfill soil in centrifuge tests on retaining wall (after Bolton and Steedman, 1985)

After rotating Fig. 12.16, symbols in (12.7) are replaced by new ones with "*",

$$P_{ae} = \frac{\gamma^* H_s^{*2}}{2} \frac{\cos^2(\phi-\beta^*)}{\cos(\delta+\beta^*)\left\{1+\sqrt{\dfrac{\sin(\phi+\delta)\sin(\phi-i^*)}{\cos(\delta+\beta^*)\cos(i^*-\beta^*)}}\right\}^2} \qquad (12.9)$$

in which $\beta^* = \beta+\psi$, $i^* = i+\psi$, $\theta_{cr}^* = \theta_{cr}+\psi$, $H_s^* = H_s$, and $\gamma^* = \frac{W^*}{W}\gamma = \frac{1-K_v}{\cos\psi}\gamma$. Consequently,

$$P_{ae} = \frac{\gamma H_s^2}{2} \frac{(1-K_v)\cos^2(\phi-\beta-\psi)}{\cos\psi\cos(\delta+\beta+\psi)\left\{1+\sqrt{\dfrac{\sin(\phi+\delta)\sin(\phi-i-\psi)}{\cos(\delta+\beta+\psi)\cos(i-\beta)}}\right\}^2} \qquad (12.10)$$

and the direction of slip plane as measured from the horizontal direction is given by

$$\cot\left(\theta_{\mathrm{cr,e}} - i\right) = -\tan\left(\beta - i + \delta + \phi\right) + \frac{1}{\cos\left(\beta - i + \delta + \phi\right)} \sqrt{\frac{\sin\left(\phi + \delta\right)\cos\left(\beta + \psi + \delta\right)}{\cos\left(\beta - i\right)\sin\left(\phi - i - \psi\right)}} \,. \tag{12.11}$$

The Mononobe–Okabe seismic active pressure acts at the elevation of 1/3 from the bottom. Recent studies recommend, however, 0.45 to 2/3 (e.g., Seed and Whitman, 1970). Figure 12.20 supports a planar slip plane as assumed by the Mononobe–Okabe theory.

Problems and further developments of the Mononobe–Okabe theory will be described in Sect. 12.8.

The Mononobe–Okabe theory is simply a product of theoretical consideration and does not have an experimental back ground. Further, there are strange attempts in which the theory is applied to situation without failure despite that the theory is a limit equilibrium one which is valid only when soil fails. With these in mind, shaking table tests were conducted on seismic earth pressure on a model of retaining wall (Watanabe et al. 1999).

Figure 12.21 illustrates a model in 1-G field in which a retaining wall is supported by an air spring and can rotate around its base. The backfill is made of air-dry (気乾) dense Toyoura sand that has 90% relative density.

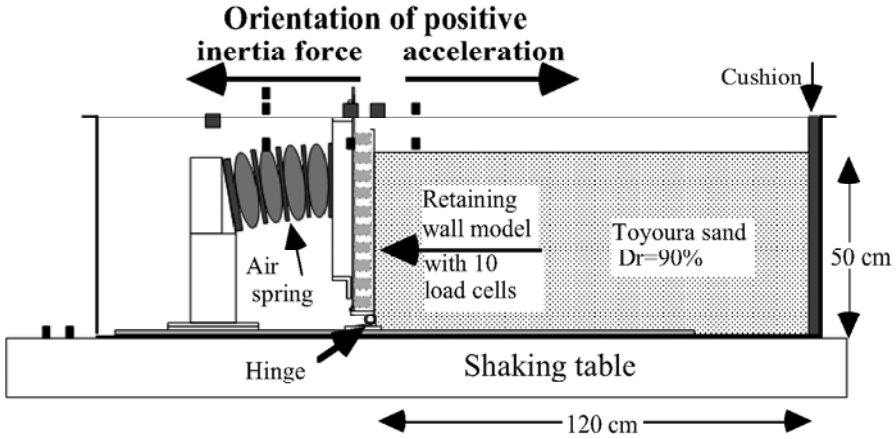

Fig. 12.21 Model of retaining wall

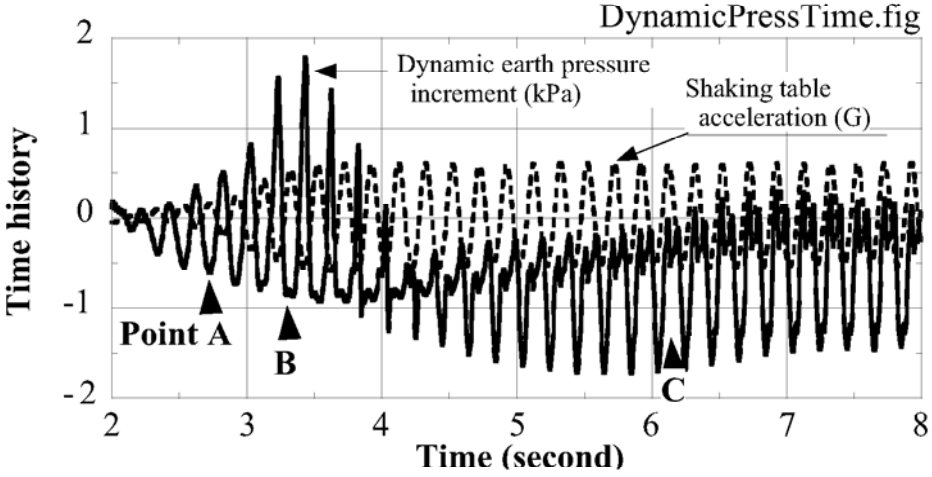

Fig. 12.22 Time history of shaking and earth pressure

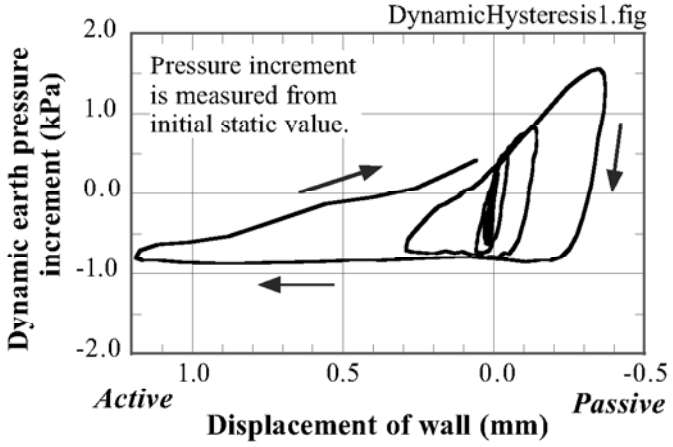

Fig. 12.23 Variation of earth pressure before failure

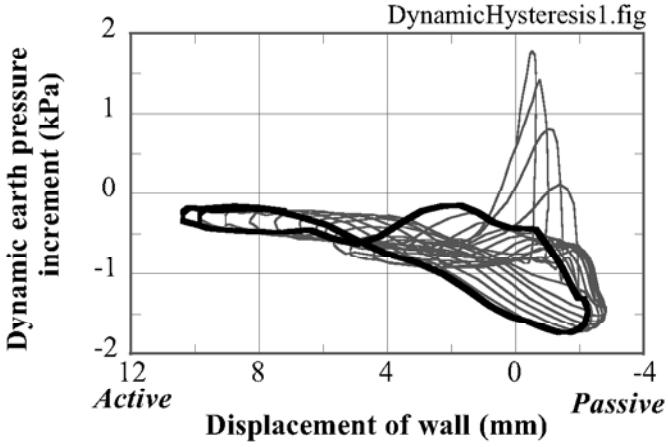

Fig. 12.24 Variation of earth pressure after failure

Figure 12.22 manifests the time history of base shaking and the dynamic increment of earth pressure. When the shaking was weak in the initial stage, the shaking and the earth pressure are 180° out of phase (逆位相 : point A). This means that the induced inertia force moved the wall outwards more than the backfill soil, leading to reduced earth pressure. This situation starts to change at around point B and, in the latest stage of point C undergoing stronger shaking, the acceleration and the earth pressure are in phase with each other (同位相). This is because the increased magnitude of shaking increased the strain amplitude, and accordingly reduced the stiffness of backfill soil (nonlinearity). Thus the soil was made easier to move than the wall. Consequently, the inertia force in the outward direction made “collision”

between soil and wall, resulting in the increased earth pressure.

Figures 12.23 and 12.24 show the relationship between the displacement of wall and the earth pressure increment during shaking. Before failure (Fig. 12.23), the earth pressure takes the maximum value when the wall moves towards the soil (positive displacement : passive state). Since the Mononobe–Okabe theory is concerned with the active state, this maximum earth pressure is out of scope of the theory. After failure (Fig. 12.24), in contrast, there is another peak earth pressure in the active state that agrees with the idea of the theory. It is noteworthy, therefore, that the Mononobe–Okabe theory assumes the wall to be more stable than the backfill soil.

Nakamura (2005) carried out centrifugal model tests (Sect. 24.11) under 30G field on dynamic earth pressure on a gravity-type retaining wall. The data hereinafter is presented in the equivalent prototype scale. Constructed models were first shaken under relatively weak intensity of motion prior to strong excitation. Figure 12.25 shows the distribution of earth pressure after this preliminary shaking. It is seen that the earth pressure had decreased to be close to the static active earth pressure probably because of minor displacement of the wall.

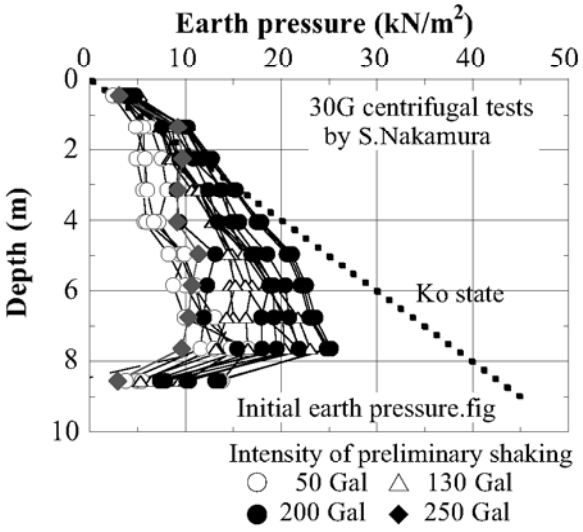

Fig. 12.25 Earth pressure distribution prior to strong shaking (after Nakamura, 2005)

Strong shaking with the maximum acceleration of 600 Gal occurred thereinafter. Figure 12.26 illustrates the relationship between the inertia force and the dynamic earth pressure when harmonic shaking occurred with 600 Gal at maximum and 2 Hz. The inertial force is taken positive when it is oriented outwards in the active direction, and the dynamic earth pressure stands for the increment of earth pressure after the initial pressure. It is shown in Fig. 12.26 that the dynamic earth pressure increment is negative when the inertial force takes the maximum value in the active direction. Thus, it may be reasonable to take the design seismic pressure equal to the initial pressure, which is equal to the static active pressure (Fig. 12.25). Furthermore in Fig. 12.27, the point of application of the earth pressure during shaking is around 25% of the wall height as shown by the data when the inertial force takes the maximum active value.

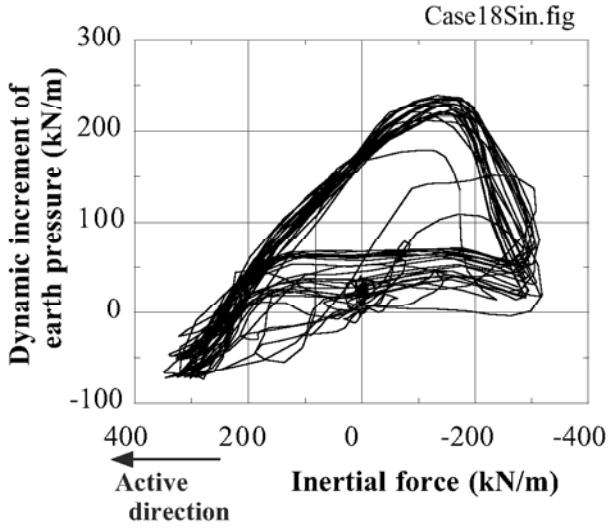

Fig. 12.26 Relationship between inertia force and earth pressure under harmonic shaking

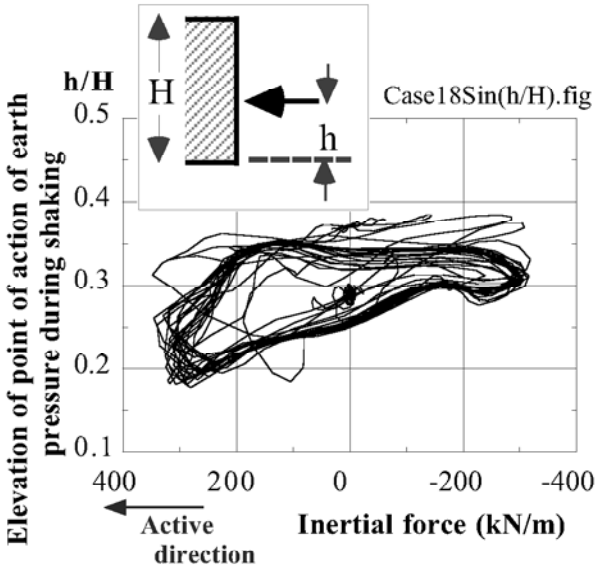

Fig. 12.27 Time change of the point of application of earth pressure during harmonic shaking

(600 Gal and 2 Hz) (data by Nakamura, 2005)

The same points can be made in Figs. 12.28 and 12.29 in which an irregular shaking of maximum 600 Gal and the predominant period of 2 Hz are employed. Thus, in contrast to the implication of Mononobe–Okabe pseudo-static theory, the static active earth pressure may be employed as the design dynamic earth pressure.

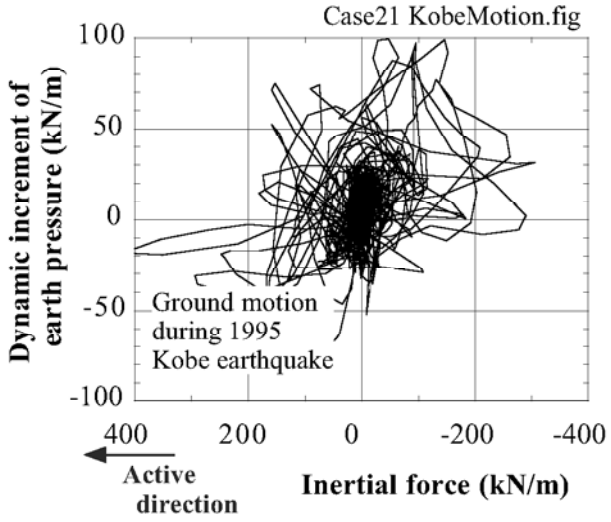

Fig. 12.28 Relationship between inertia force and earth pressure under irregular shaking (600 Gal and 2 Hz) (data by Nakamura, 2005)

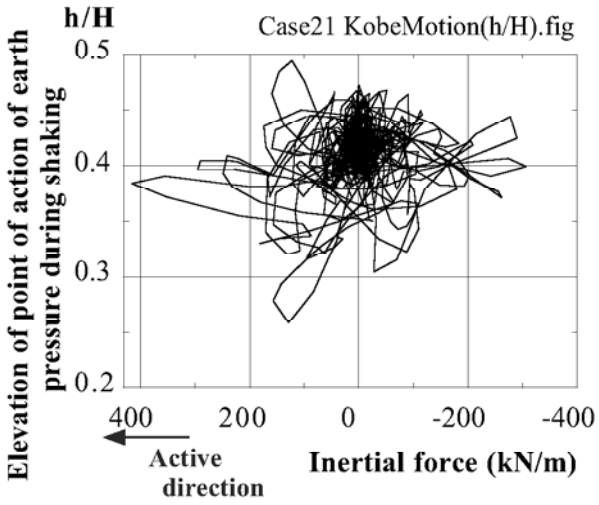

Fig. 12.29 Time change of the point of application of earth pressure during irregular shaking (600 Gal and 2 Hz) (data by Nakamura, 2005)

12.7 Comparison of Static and Seismic Active Earth Pressures

It is intended here to compare the seismic active earth pressure as derived by the *Mononobe–Okabe* formula with the *Coulomb* static active earth pressure. Fig. 12.30 illustrates the concerned situation in which the face of a wall is smooth ($\delta = 0$) and vertical ($\beta = 0$), while the surface of the backfill is level ($i = 0$). The *Mononobe–Okabe* seismic active earth pressure is then given by

$$P_{ae} = \frac{K_{ae}}{2}\gamma H^2, \tag{12.12}$$

where the earth pressure coefficient, K_{ae}, is given by

$$K_{ae} = \frac{\cos^2(\phi - \psi)}{\cos\psi\left\{1 + \sqrt{\dfrac{\sin\phi\sin(\phi - \psi)}{\cos\psi}}\right\}^2}. \tag{12.13}$$

The static active earth pressure, on the other hand, is given by

$$P_a = \frac{K_a}{2}\gamma H^2 \tag{12.14}$$

wherein

$$K_a = \tan^2\left(45° - \frac{\phi}{2}\right). \tag{12.15}$$

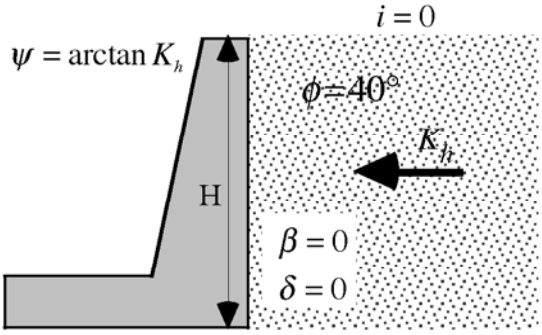

Fig. 12.30 Illustration of studied retaining wall model

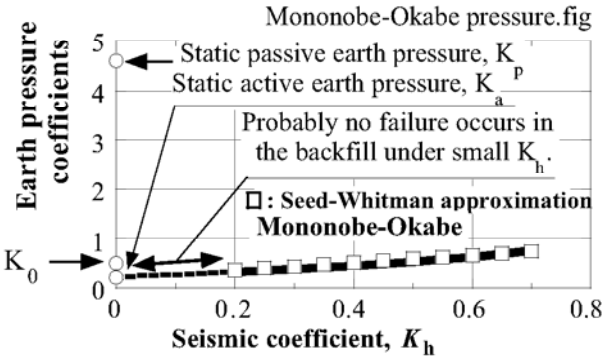

Fig. 12.31 Comparison of Mononobe–Okabe seismic active earth pressure coefficient with static earth pressure coefficients

Moreover, the coefficients of static earth pressure at rest (K_0) and of passive earth pressure, $K_p = \tan^2\left(45° + \frac{\phi}{2}\right)$, are going to be studied.

Figure 12.31 compares three kinds of static earth pressure coefficients, K_a, K_o, and K_p, with K_{ae}, which varies with the seismic coefficient of K_h. The friction angle of 40° is assumed in the backfill soil. In Fig. 12.31, following points are made:

1. K_a is less than K_o that is around 0.5 for normally consolidated soils.
2. K_{ae} increases from K_a as K_h increases. However, K_{ae} is still less than K_0 when K_h is relatively small.
3. Since small values of K_h cannot induce a state of limit equilibrium, the calculated K_{ae} with small K_h is not meaningful. Hence, a dashed curve is employed in the figure.

Seed and Whitman (1970) used $\phi = 35°$ and proposed an approximate expression of

$$K_{ae} = K_a + \frac{3}{4}K_h. \tag{12.16}$$

This approximation is shown also in Fig. 12.31 by a symbol of □. Its matching with the original Mononobe–Okabe formula is good in spite of different friction angles of 35° and 40° employed.

Since 1990s, there has been a strong trend to increase the design seismic coefficient due to experiences of strong earthquake motions (see Fig. 14.20) and importance of structures. Consequently, the seismic coefficient is increasing from former levels of, for example, $K_h = 0.20$ to stronger levels such as 0.5 or more. Another issue is the use of friction angle at the residual deformation, $\phi_{residual}$, rather than that at the peak strength, ϕ_{peak}. As Fig. 12.32 illustrates conceptually, the residual friction angle is smaller than the peak friction angle and gives a conservative (higher) earth pressure coefficient. For experimental data, see Fig. 1.15.

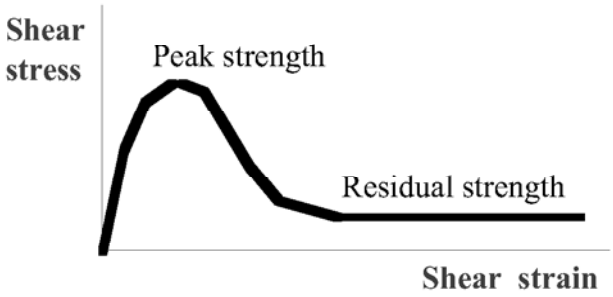

Fig. 12.32 Schematic illustration of peak and residual shear strength

Those greater values of K_h were substituted in (12.10) and (12.11) to calculate the seismic earth pressure coefficient, K_{ae}, and the direction of the slip plane, $\theta_{cr,e}$. The direction of the slip plane is measured from the horizontal direction; see (12.17) and (12.18).

$$K_{ae} = \frac{(1-K_v)\cos^2(\phi-\beta-\psi)}{\cos\psi\cos(\delta+\beta+\psi)\left\{1+\sqrt{\dfrac{\sin(\phi+\delta)\sin(\phi-i-\psi)}{\cos(\delta+\beta+\psi)\cos(i-\beta)}}\right\}^2}, \tag{12.17}$$

$$\cot(\theta_{cr,e}-i) = -\tan(\beta-i+\delta+\phi)+\frac{1}{\cos(\beta-i+\delta+\phi)}\sqrt{\frac{\sin(\phi+\delta)\cos(\beta+\psi+\delta)}{\cos(\beta-i)\sin(\phi-i-\psi)}}. \tag{12.18}$$

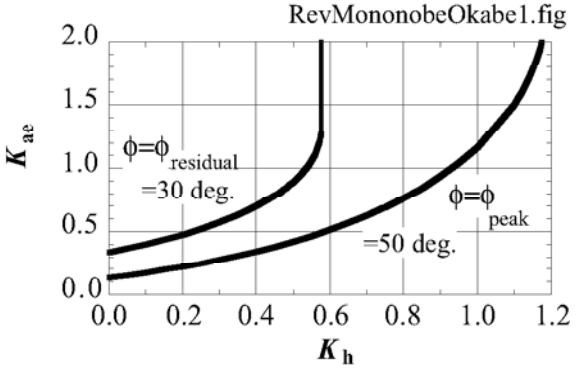

Fig. 12.33 Seismic earth pressure coefficient by conventional Mononobe–Okabe theory

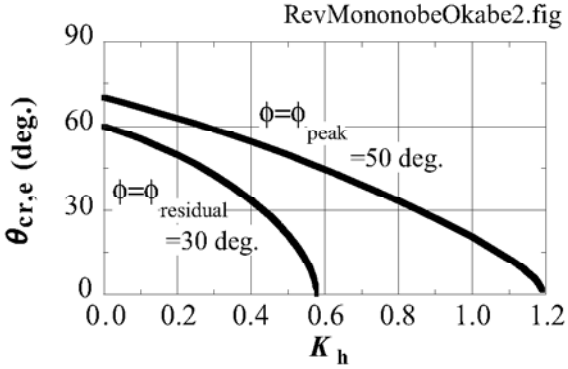

Fig. 12.34 Direction of seismic slip plane calculated by conventional Mononobe–Okabe theory

In this calculation, $\psi = \arctan\{K_h/(1-K_v)\}$, while $K_v = 0$ and $\beta = i = \delta = 0$ is assumed for simplicity. The calculated results in Figs. 12.33 and 12.34 employed ϕ_{peak} and $\phi_{residual}$ being 50° and 30° respectively. Accordingly,

1. The earth pressure that was increased by the residual strength is conservative but makes retaining walls more costly,
2. When K_h exceed 0.6, the earth pressure with $\phi_{residual}$ becomes infinite and design calculation is made impossible, and
3. This problem is accompanied by the direction of slip plane, which becomes nearly horizontal (Fig. 12.35).

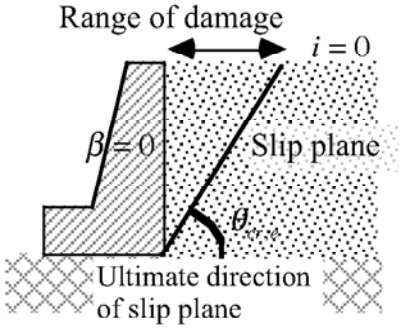

Fig. 12.35 Negative orientation of slip plane calculated by conventional Mononobe–Okabe theory

To overcome this problem and to assess a reasonable magnitude of seismic earth pressure under strong design earthquake and $\phi_{residual}$, Koseki et al. (1998) proposed a modified Mononobe–Okabe theory. They

conducted 1-G shaking tests on a model of a gravity-type quay wall with dense sandy backfill (Toyoura sand of relative density = 80%). Shaking was conducted by using the motion that was recorded at Kobe Meteorological Observatory in 1995. This shaking was repeated several times by increasing the amplitude.

Fig. 12.36 Development of first slip plane after shaking with maximum acceleration = 513 Gal (Photo by K. Watanabe)

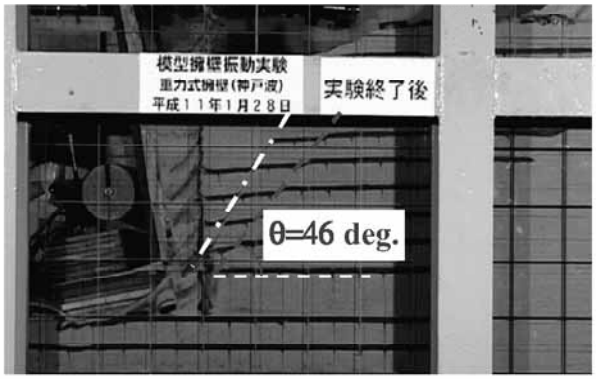

Fig. 12.37 Development of second slip plane after shaking with maximum acceleration = 919 Gal (Photo by K. Watanabe)

Figure 12.36 illustrates the appearance of a model after shaking with the maximum acceleration of 513 Gal. The orientation of the developed slip plane was 54°. Shaking was further conducted on the same model, while maintaining the first slip plane unchanged. After shaking at 919 Gal (Fig. 12.37), the second slip plane developed in the direction of 46°. Consequently, the new earth pressure theory was constructed as what follows:

1. The first failure mechanism (slip plane) is determined by ϕ_{peak} under minor magnitude of seismic coefficient (K_h = 0.0 or 0.2 for design practice);
   in case of $\phi_{peak} = 50°$ and $K_h = 0$ together with $\beta = i = \delta = K_v = 0$, for example, K_{ae} = 0.132 and $\theta_{cr,e} = 70°$.
2. Under stronger seismic loads ($K_h > 0$), the seismic active earth pressure is produced by this mechanism ($\theta = 70°$), but the friction angle along this plane is reduced to $\phi_{residual}$. Because of this reduced friction angle, the earth pressure is increased. Note that the friction angle in other parts of the backfill is still kept at ϕ_{peak}. Figure 12.38 compares earth pressure coefficients obtained by the conventional Mononobe–Okabe theory and this modified idea. The increased earth pressure is still less than the pressure calculated by Mononobe–Okabe theory with $\phi_{residual}$.

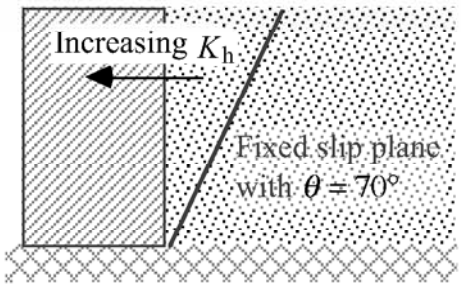

Calculation of modified seismic earth pressure

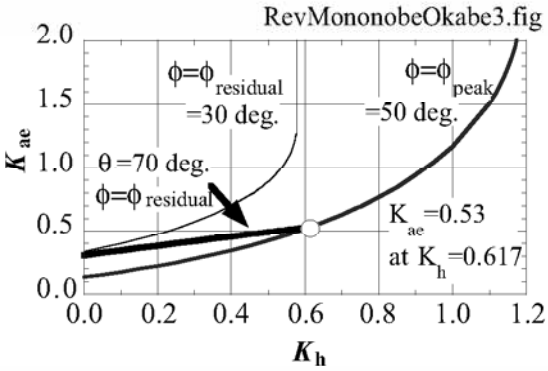

Fig. 12.38 Comparison of conventional Mononobe–Okabe seismic earth pressure and the pressure obtained by fixed slip plane under increasing K_h

3. As Fig. 12.38 indicates, the modified theory and the conventional Mononobe–Okabe theory with $\phi_{peak} = 50°$ give the same results at K_h = 0.617. This implies that the entire backfill is subject to failure again. The conventional Mononobe–Okabe theory with $\phi_{peak} = 50°$ and K_h = 0.617 gives

$\theta_{cr,e} = 43.6°$

4. After $K_h = 0.617$, the second failure mechanism plays a chief role in the direction of $\theta = 43.6°$ together with $\phi_{residual} = 30°$. This feature is illustrated in Fig. 12.39.

The modified Mononobe–Okabe theory maintains θ angle at a constant value while K_h value increases. This is in a good contrast with the conventional theory in which θ decreases with increasing K_h (Fig. 12.34). Thus, the range of damage in Fig. 12.35 ($H/\tan\theta$) is made smaller by the modified theory. This is a good advantage because the need for soil improvement in the backfill is reduced.

Note that the earth pressure calculation in the modified theory depends on the initial determination of the slip plane orientation. In the example above, this orientation was determined at $K_h = 0$. There is no definite reason, however, to support this practice, and engineering judgement is required in this respect.

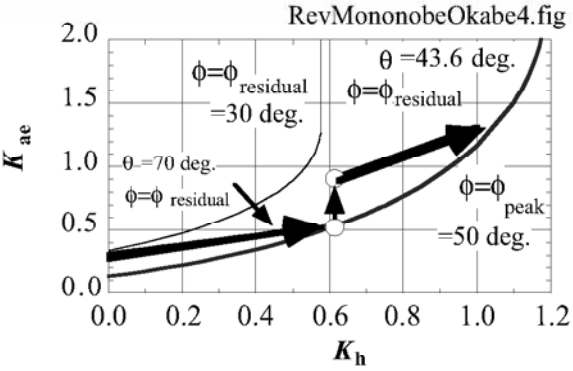

Fig. 12.39 Seismic earth pressure activated after second development of slip plane

List of References in Chapter 12

Bolton, M.D. and Steedman, R.S. (1985) Modelling the seismic resistance of retaining structures, Proc. 11th Int. Conf. Soil Mech. Found. Eng., Vol. 4, pp. 1845–1848.

Koseki, J., Tatsuoka, F., Munaf, Y., Tateyama, M. and Kojima, K. (1998) A modified procedure to evaluate active earth pressure at high seismic loads, Soils and Foundations, Special Issue No.2 on Geotechnical Aspects of the January 17 1995 Hyogoken-Nambu earthquake, pp. 209–216.

Mononobe, N. (1924) Discussion and consideration on vertical earthquake motion and consideration, Proc. JSCE, Vol. 10, No. 5, pp. 1063–1095 (in Japanese).

Mononobe, N. and Matsuo, H. (1929) On the determination of earth pressure during earthquakes, Proc. World Engineering Conference, Vol. 9, pp. 177–185.

Nakamura, S. (2005) Clarification of seismic behavior of gravity retaining wall by using centrifugal model tests and a proposal for rationalization of the seismic coefficient method. Proc. JSCE, 785/III-70, pp. 107–122 (in Japanese).

Newmark, N.M. (1965) Effects of earthquakes on dams and embankments, Geotech., Vol. 5, No. 2, pp. 137–160.

Noda, S., Uwabe, T. and Chiba, T. (1975) Relation between seismic coefficient and ground acceleration for gravity quaywall 重力式岸壁の震度と地盤加速度, Report of the Port and Harbor Research Institute 港湾技術研究所報告,Vol. 14, No. 4, pp. 67–111 (in Japanese).

Ohmachi, T., Toshinawa, T. and Yasuhara, M. (1990) Earthquake sliding response spectrum and its application, Proc. 8th Jpn. Earthq. Eng. Symp., pp. 981–986, Tokyo (in Japanese).

Okabe, S. (1924) General theory on earth pressure and seismic stability of retaining wall and dam. Proc. JSCE, Vol. 10, No. 6, pp. 1277–1330 (in Japanese).

Okabe, S. (1926). General theory of earth pressure and laboratory testings on seismic stability of retaining walls, Proc. JSCE, Vol. 12, No. 1, pp. 123–134 (in Japanese).

Seed, H.B. and Whitman, R.V. (1970) Design of earth retaining structures for dynamic Loads, Lateral Stresses in the Ground and Design of Earth-Retaining Structures, ASCE, pp. 103–147.

Watanabe, K., Maeda, T., Kobayashi, Y. and Towhata, I. (1999) Shaking table tests on seismic earth pressure exerted on retaining wall model, Proc. 2nd International Conference on Earthquake Geotechnical Engineering, Vol. 1, Lisbon, pp. 297–302.